Title: Porous microwells for geometry-selective, large-scale particle arrays

Jae Jung Kim[1†], Ki Wan Bong[2,3†], Eduardo Reátegui[2,4], Daniel Irimia[2*], and Patrick S. Doyle[1*]

Affiliations:

[1]Department of Chemical Engineering, Massachusetts Institute of Technology, Cambridge, MA, 02139, USA.

[2]BioMEMS Resource Center, Massachusetts General Hospital, Harvard Medical School, and Shriners Hospital for Children, MA, 02129, USA.

[3]Department of Chemical and Biological Engineering, Korea University, 02841, South Korea.

[4]Massachusetts General Hospital Cancer Center, Harvard Medical School, MA, 02129, USA.

*Correspondence to:

Patrick S. Doyle (pdoyle@mit.edu), Daniel Irimia (dirimia@mgh.harvard.edu)

†These authors contributed equally to this work.

Table of Contents

Prepolymer compositions. For PEG-DA particles, up to 45 % PEG-DA, prepolymer composition was x % PEG-DA (Sigma Aldrich, Mn = 700), (55-x) % (v/v) PEG (Sigma Aldrich, Mn = 200), 40 % (v/v) 3×tris-EDTA (TE), 5 % (v/v) 2-hydroxy-2-methylpropiophenone (Sigma Aldrich, photo-initiator, PI). 70 % PEG-DA prepolymer solution was 70 % (v/v) PEG-DA (Sigma Aldrich, Mn = 700), 10 % (v/v) PEG (Sigma Aldrich, Mn = 200), 15 % (v/v) 3×TE, 5 % (v/v) PI. Fluorescence is given by fluorescent microsphere (Polyscience, Inc., carboxylated YG, diameter = 0.2 µm) dispersed in water, and 1mg/ml rhodamine acrylate (Polyscience, Inc.) in PEG (Mn = 200) with 1 % (v/v) ×100 TE (**Table S1**). For UCN-laden microparticles, 50 % (v/v) PUA (MINS-311RM, Minuta Technology), 40 % (v/v) acrylic acid (Polyscience, Inc.), 10 % PI were mixed, and this mixture is added to dried UCNs in order to make prepolymer solution (concentration of UCNs is given in **Table S2**).

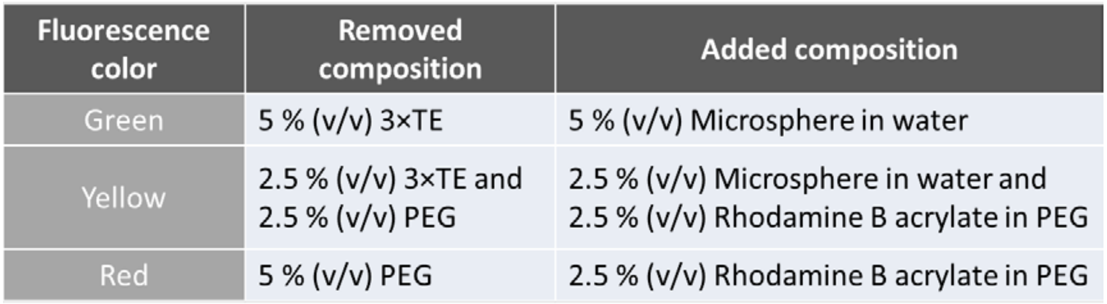

Fluorescence color	Removed composition	Added composition
Green	5 % (v/v) 3×TE	5 % (v/v) Microsphere in water
Yellow	2.5 % (v/v) 3×TE and 2.5 % (v/v) PEG	2.5 % (v/v) Microsphere in water and 2.5 % (v/v) Rhodamine B acrylate in PEG
Red	5 % (v/v) PEG	2.5 % (v/v) Rhodamine B acrylate in PEG

Table S1. Replaced composition of PEG-DA prepolymer solution for fluorescence.

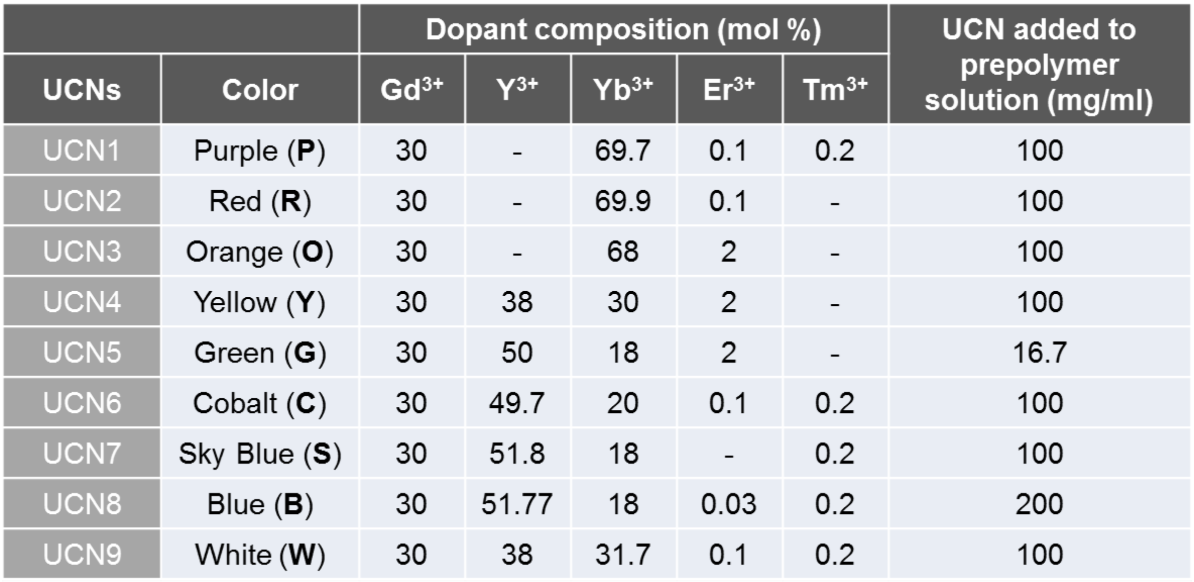

		Dopant composition (mol %)					UCN added to prepolymer solution (mg/ml)
UCNs	Color	Gd^{3+}	Y^{3+}	Yb^{3+}	Er^{3+}	Tm^{3+}	
UCN1	Purple (**P**)	30	-	69.7	0.1	0.2	100
UCN2	Red (**R**)	30	-	69.9	0.1	-	100
UCN3	Orange (**O**)	30	-	68	2	-	100
UCN4	Yellow (**Y**)	30	38	30	2	-	100
UCN5	Green (**G**)	30	50	18	2	-	16.7
UCN6	Cobalt (**C**)	30	49.7	20	0.1	0.2	100
UCN7	Sky Blue (**S**)	30	51.8	18	-	0.2	100
UCN8	Blue (**B**)	30	51.77	18	0.03	0.2	200
UCN9	White (**W**)	30	38	31.7	0.1	0.2	100

Table S2. UCNs' dopant composition and concentration in prepolymer solution

Upconversion nanocrystal synthesis. Upconversion nanocrystals are synthesized via hydrothermal method as described previously[1]. 3 ml of NaOH (Macron) aqueous solution (0.2 g/ml), 10 ml of ethanol (Koptec), and 10 ml of oleic acid (Sigma Aldrich) are mix under stirring. 4 ml of $RECl_3$ (0.2 M, RE = Y, Yb, Gd, Er, Tm, Aldrich, 99.9 %, **Table S2** for composition) and 2 ml of NH_4F (2M, Sigma Aldrich) were added dropwise. Mixture is transferred Teflon-lined autoclave and heated at 200 °C for 4 h in the oven. After cooling at room temperature, synthesized UCNs were purified with ethanol and water repeatedly by centrifugation, and stored in cyclohexane.

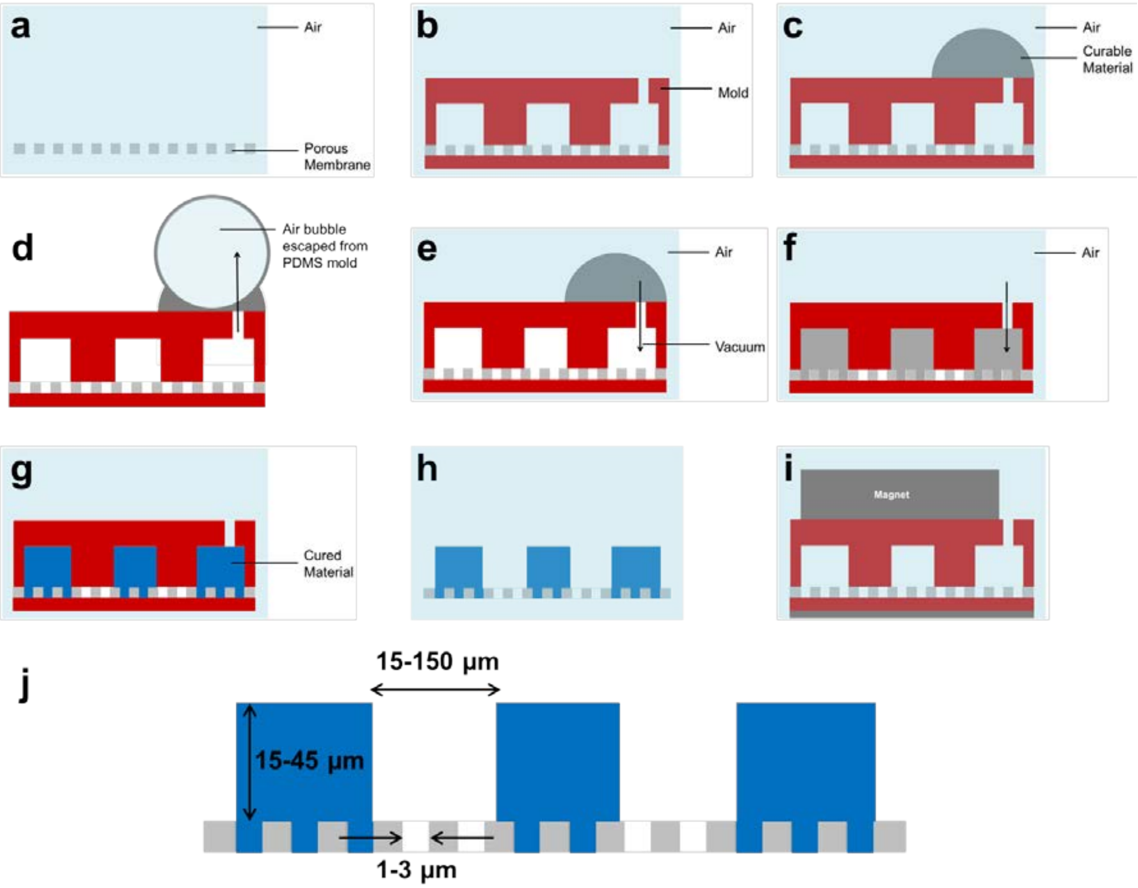

Figure S1. Detail schematic for fabrication of porous microwell arrays. a, A porous PET membrane is prepared. **b**, PDMS mold and flat PDMS film are placed at top and bottom of the membrane, respectively. **c**, Curable material is placed on top of the inlet of PDMS mold. **d**, Vacuum is applied to whole platform to remove the air trapped in PDMS mold. Escaped air forms a bubble and then pops. **e**, Vacuum is removed, and atmospheric pressure is recovered outside the PDMS mold while vacuum is maintained inside the PDMS mold. **f**, Curable material is injected into the PDMS mold due to the pressure difference. **g**, Curable material is cured. **h**, PDMS mold and flat PDMS are detached. Porous microwell arrays are fabricated. **i**, In step **b**, placing magnets at the top and the bottom of the platform helps to ensure good contact. This magnetic compression method was used for thermally curable materials (PDMS, epoxy, and polyester). **j**, Dimensions of porous microwell arrays. The geometry of the porous microwells can be engineered over a wide range. Unless otherwise indicated, results shown in this study utilized 35 μm microwell height and 3 μm diameter pores.

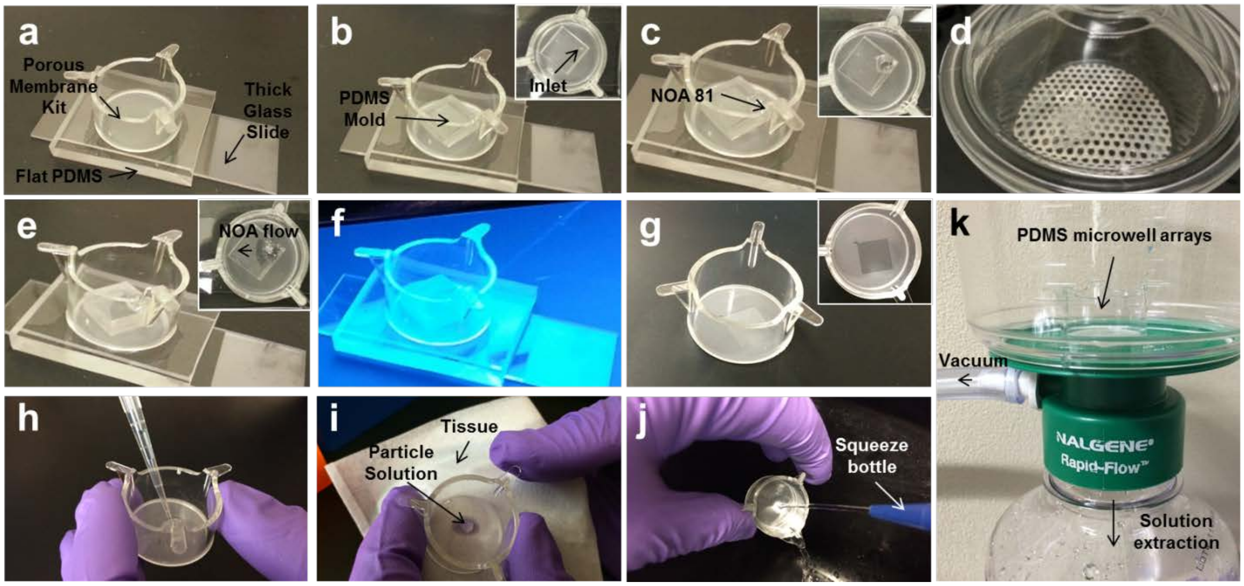

Figure S2. Procedure for microwell fabrication and microparticle assembly. a, Assemble flat PDMS at the bottom of porous membrane kit. **b**, Assemble PDMS mold on top of porous membrane. **c**, Drop the curable material (NOA 81) on top of inlet. **d**, Apply the vacuum. **e**, Remove the vacuum, and wait until curable material fills the mold. **f**, Cure the curable materials (UV exposure for NOA 81). **g**, Disassemble PDMS mold and flat PDMS, getting porous microwell arrays. **h**, Drop the particle solution. **i**, Assemble the particle into a microwell. For NOA microwells, negative pressure is driven by capillary/wetting. Applied pressure is calculated by measuring the volumetric flow rate (=dropped solution volume/time) through the porous microwells. **j**, Wash the redundant particles. **k**, For PDMS microwells, vacuum is applied to generate the negative pressure for particle assembly.

Selection of porous PET membrane

In order to have open pores inside the microwell, pores in the membrane should meet two requirements: 1. Density of pores should be high enough. 2. Pores should not be connected to each other. If pore density is low, each microwell is statistically not able to have a pore. If one pore is connected to another, curable materials can penetrate to the pore under the microwell mold even though mold and membrane have good contact (**Fig. S3**). While satisfying the above two requirements of porous membrane, it is also desired to have a larger pore size. This is because larger pores result in faster flow toward the porous microwell, ensuring better guiding of microparticles to microwells. Among the commercially available PET membranes (**Fig. S4**), the porous membrane with d = 3.0 µm from Millipore satisfied the aforementioned requirements and have the maximum pore size.

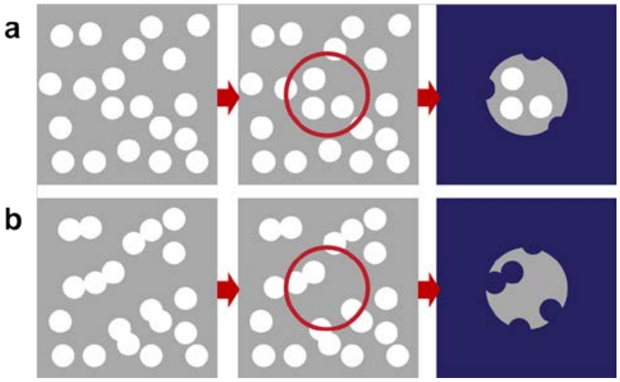

Figure S3. Importance of pore isolation for porous microwell fabrication. a, A membrane which has isolated pores and **b,** a membrane which has connected pores. Left images show the porous PET membrane. Red circle in middle images represents the location of microwell. Right images show the fabricated porous microwells. White and blue pores represent open and close pore, respectively.

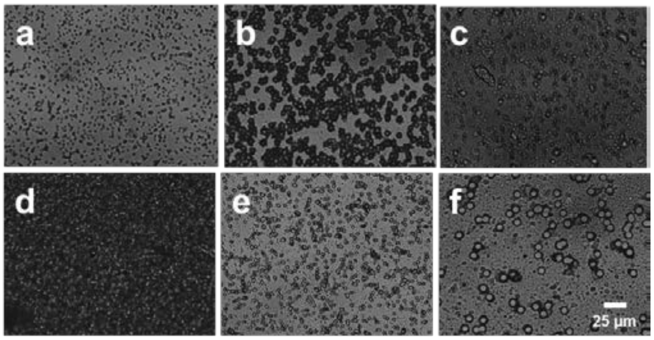

Figure S4. Commercially available porous PET membranes. a, Pore diameter d = 0.4 µm from Corning. **b,** d = 3.0 µm from Corning. **c**, d = 1.0 µm from Greiner bio-one. **d,** d = 0.4 µm from Millipore. **e,** d = 3.0 µm from Millipore. **f,** d = 8.0 µm from Millipore. Dark region represents the edge of pores, and the diameter of pore is based on the specification from the vendor.

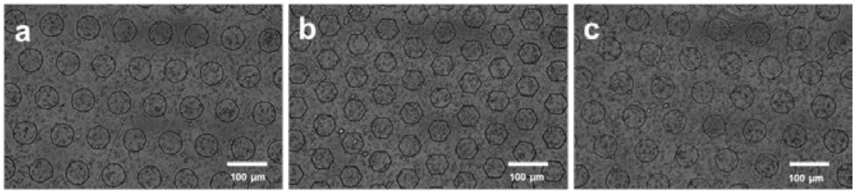

Figure S5. Porous microwells made by a variety of photo-curable materials. a, Cylindrical porous microwells made by 90 % (v/v) PUA and 10 % (v/v) PI. **b**, Porous microwells with hexagonal top made by 90 % (v/v) PEG(200)-DA (Polyscience, Inc.) and 10 % (v/v) PI. c, Cylindrical porous microwells made by 65 % (v/v) 1-(acryloyloxy)-3-(methacryloyloxy)-2-propanol (Polyscience, Inc.), 30 % (v/v) 2-hydroxyethyl acrylate (Sigma Aldrich), and 5 % (v/v) PI.

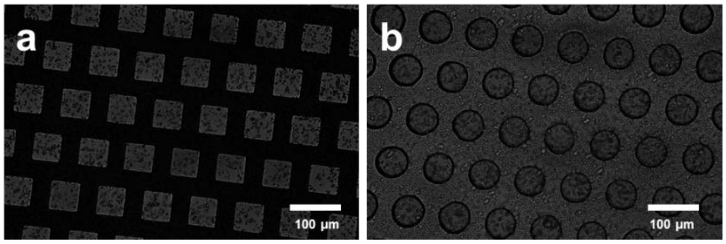

Figure S6. Porous microwells made by a variety of thermal-curable materials. a, Porous microwell arrays with square top made by epoxy (3M Scotch-Weld, DP 270 black). **b**, Cylindrical porous microwells made by polyester casting resin (Castin' craft, resin and catalyst were mixed at 9:1 (w/w) ratio).

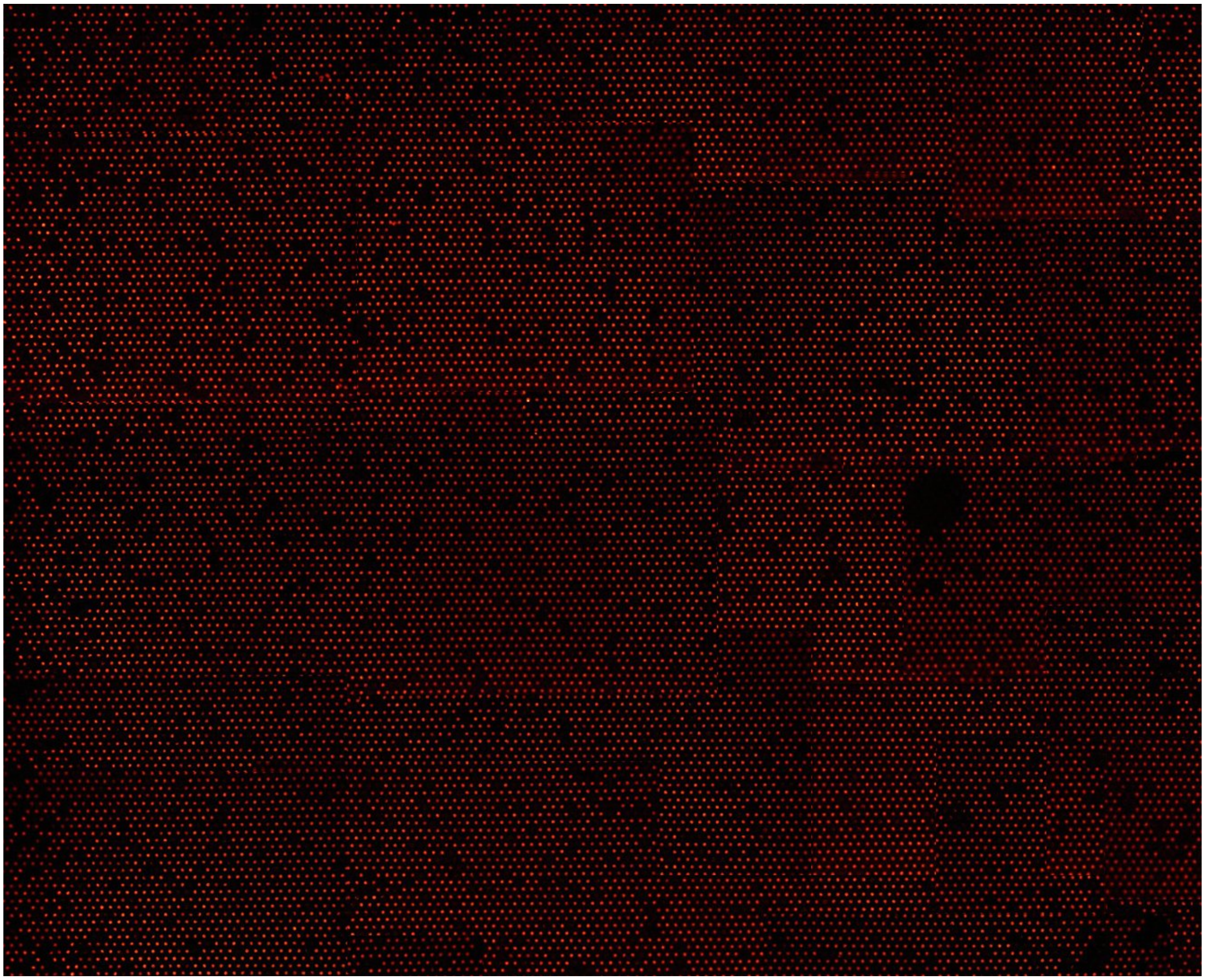

Figure S7. The largest-scale particle assembly. ~ 15000 particles (~30 µm) were assembled into microwells.

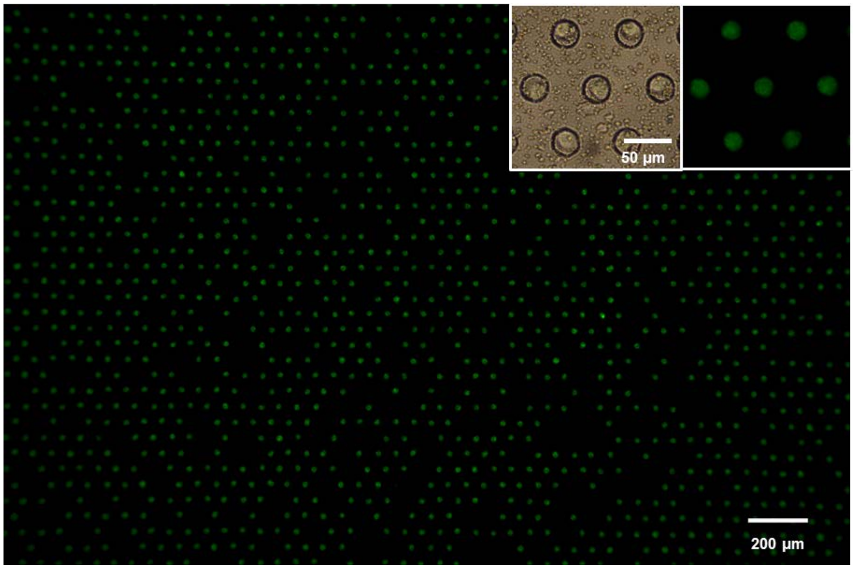

Figure S8. Large-scale array of microparticles with smaller diameter than microwells. Microparticles were not squeezed due to the smaller diameter, so there was no radial normal stress. Therefore, some assembled particles were removed during the washing step, resulting lower yield on filling wells (83 %) than **Fig. 1h** (94 %). Shear protection due to the depth of microwells makes assembled particles maintain their positions. Inset shows the closed view of bright field (left) and fluorescent (right) images.

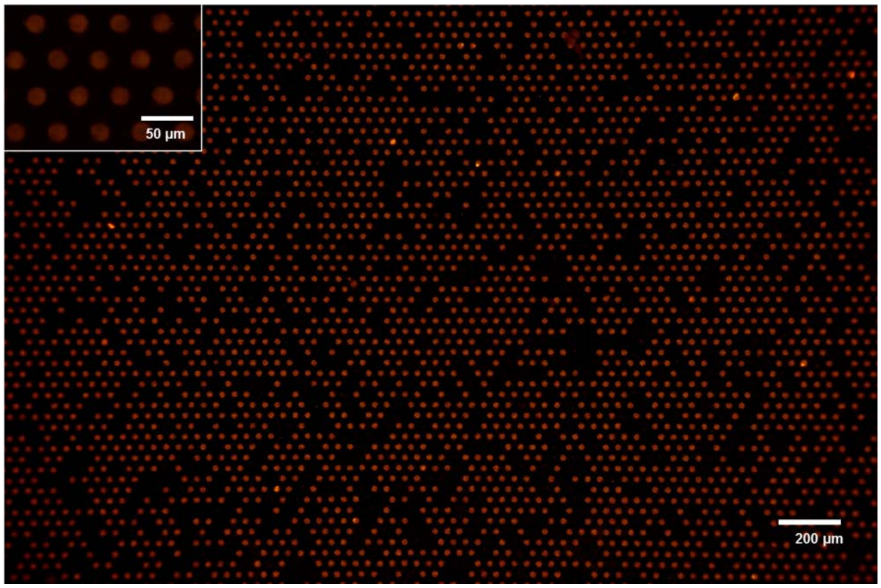

Figure S9. 20 μm particle assembly. ~ 76% of microwells were filled with microparticles. Microwell arrays were made with porous PET membrane (d = 3.0 μm, Millipore, **Fig. S4e**). Height of microwell (H_w) and particle (H_p) are 19 μm.

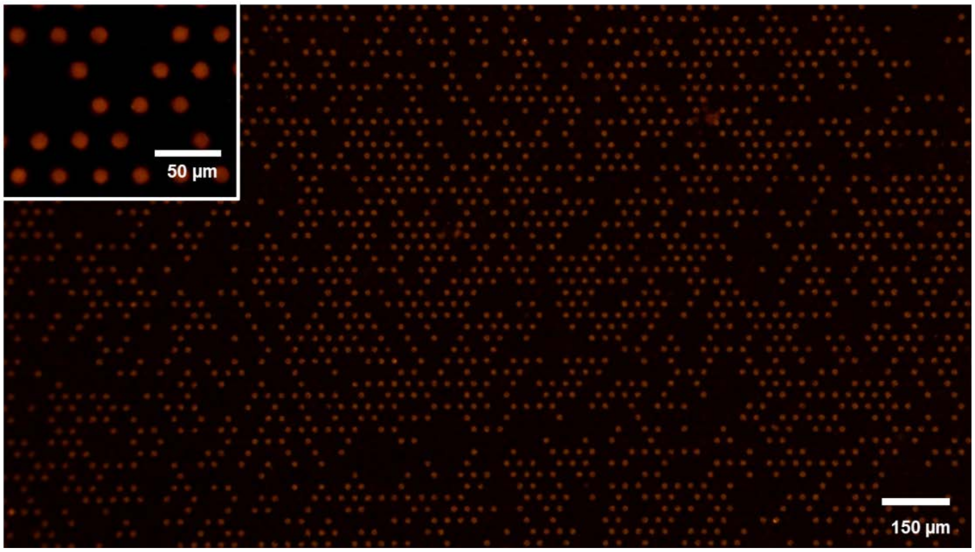

Figure S10. 15 µm particle assembly. ~ 49 % of microwells were filled with microparticles. Microwell arrays were made with porous PET membrane (d = 1.0 µm, Greiner bio-one, **Fig. S4c**). Height of microwell (H_w) and particle (H_p) are 15 µm.

Derivation of scaling analysis

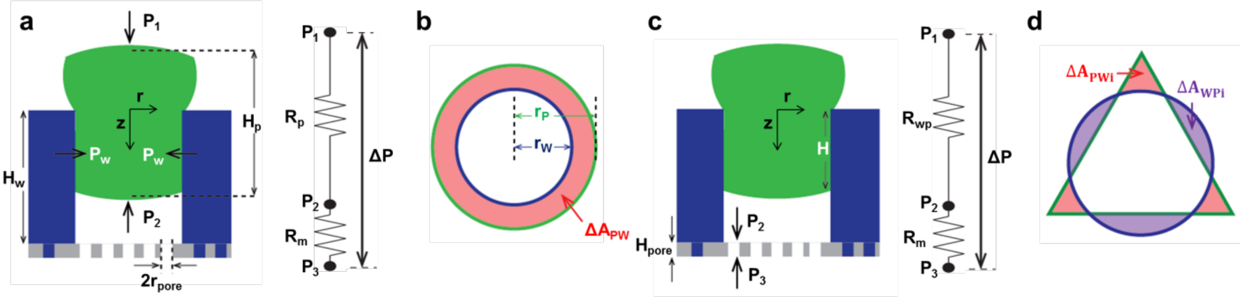

Figure S11. Close view of schematics of scaling analysis: Shape matched (**a**,**b**) and shape mismatched cases (**c**,**d**) at side (**a**,**c**) and top views (**b**,**d**).

As shown in **Fig. S11**, which shows the middle status of particle assembly, a microwell is assumed not to deform during the particle assembly process; the modulus of microparticle is much smaller than that of microwells in all cases of this project. Consider first forces acting on the microparticle in the shape matched case (**Fig. S11a, b**). The force originated from the pressure difference across the particle (F_P) is balanced with the friction between the particle and the wall of microwell (F_F); wall pressure (P_w) is normal to the wall, and because the wall is assumed to have a zero tapered angle, the z component of P_w is zero. Interference fit^2 and capillary micromechanics[3, 4], which are analogous to the particle assembly process, allow F_P and F_F to be simply scaled as

$$F_P \sim (P_1 - P_2)\,\bar{r}^2 \tag{1}$$

$$F_F \sim \int \mu P_w \, dA_{contact} \sim \int \mu P_w H \, dl_{contact} \tag{2}$$

where P_1 and P_2 are the pressure at the top and bottom of microparticle, $\bar{r}$ is the radius of particle averaged along the z direction, and μ is the friction coefficient between particle and microwell. Considering the area where the particle contact with the microwell, $A_{contact}$ is the total area, H is the vertical length, and $l_{contact}$ is the length of perimeter of cross section (**Fig. S13**). Microparticles are assembled when F_P is larger than F_F. As the particle is assembled (i.e., H increases, and $\bar{\bar{r}}$ decreases), the ratio of F_P to F_F decreases. To judge whether particle can be assembled, it is reasonable to consider only the point where the ratio of F_P to F_F is minimized. Thus, we consider only the last moment of assembly process when the particle is about to touch the porous membrane at the bottom of microwell (**Fig. S12**).

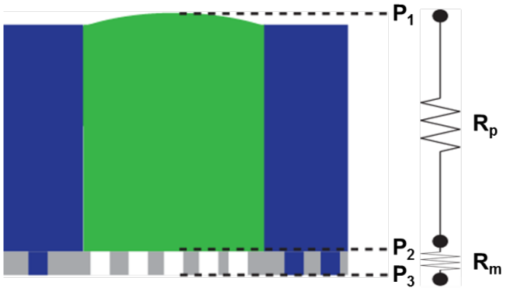

Figure S12. Schematic showing the final status of the particle assembly process. At this point, the ratio of F_P to F_F is minimized. A schematic indicating the pressure and hydrodynamic resistance is shown.

Pressure difference across the platform $(P_1 - P_3)$ is

$$P_1 - P_3 = (P_1 - P_2) + (P_2 - P_3) = \Delta P \tag{3}$$

where P_3 is the pressure at the bottom of porous membrane, and ΔP is the applied pressure difference. Consider the hydrodynamic resistance along the z direction. The resistance of microparticle (R_P) is much larger than that of porous membrane (R_M); there is no gap between microparticle and microwell, and microparticle have much smaller pore size than membrane ($r_{pore} = 1.5\ \mu m$). In other word, pressure difference across the particle ($P_1 - P_2$) is much larger than that across the membrane ($P_2 - P_3$). Therefore,

$$P_1 - P_2 \cong \Delta P \tag{4}$$

The cross sections of microparticle and microwell are assumed to be close to the circle. Thus, the characteristic radius of microwell (r_w) and microparticle (r_p) is given by

$$r_w = \sqrt{A_w/\pi} \tag{5}$$

$$r_p = \sqrt{A_p/\pi} \tag{6}$$

where A_w and A_p are the cross section area of microwell and microparticle. Note that r_w is smaller than r_p. Thus, at the last moment of assembly, the average radius of particle ($\bar{r}$) is

$$\bar{r} \cong r_w \tag{7}$$

Substituting Eqs. (4) and (7) into Eq. (1) gives

$$F_P \sim \Delta P\ {r_w}^2 \tag{8}$$

Wall pressure (P_w) is originated from the particle deformation (δ_p), where E_p is a particle (compressive) modulus, and v_p is the Poisson ratio of microparticle ($1 - v_p \sim 1$).

$$P_w \sim \frac{E_p \delta_p}{r_p(1-v_p)} \sim \frac{E_p \delta_p}{r_p} \tag{9}$$

At the last moment of assembly, H becomes the smaller one among microwell (H_w) and microparticle height (H_p). In all cases, H_p is smaller than H_w in this study.

$$H = \min(H_w, H_p) = H_p \tag{10}$$

Substituting Eqs. (9) and (10) into Eq. (2) gives

$$F_F \sim \int \mu P_w H\, dl_{contact} \sim \int \mu \frac{E_p \delta_p}{r_p} H_p\, dl_{contact} \tag{11}$$

μ, E_p, and H_p are considered as constant. Also, as mentioned, the cross section of particle is close to one, resulting r_p constant during the integration.

$$F_F \sim \frac{\mu E_p H_p}{r_p} \int \delta_p \, dl_{contact} \qquad (12)$$

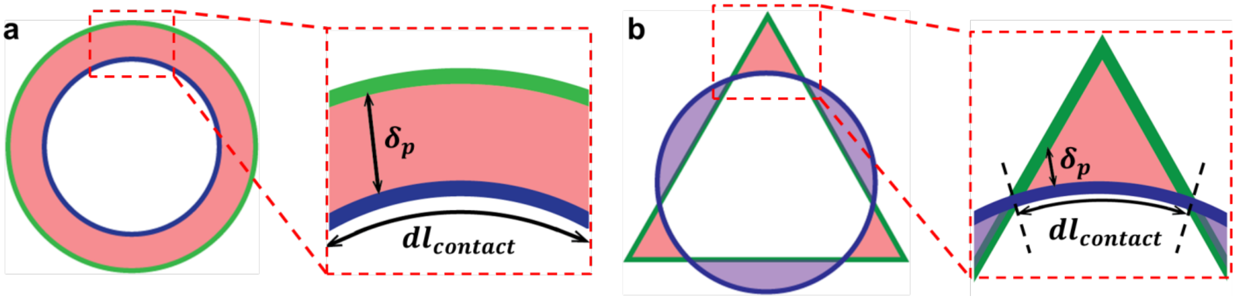

Figure S13. Integration of particle deformation (δ_P) over the contact length ($l_{contact}$): Shape matched (**a**) and shape (**b**) mismatched cases at top views.

Integrating δ_p over the $l_{contact}$ gives the cross section of particle which stick out from the cross section of microwell ($\sum_i \Delta A_{pwi} = \Delta A_{pw}$).

$$\int \delta_P dl_{contact} \sim \Delta A_{pw} \qquad (13)$$

Note that Eq. (13) is valid for both shape matched and mismatched cases (**Fig. S13**). Substituting Eqs. (13) into (12) gives

$$F_F \sim \frac{\mu E_p H_p}{r_p} \Delta A_{pw} \qquad (14)$$

The dimensionless number (Ψ) governing the assembly process is the ratio of the driving force originated from pressure difference to the wall friction. Combining Eqs. (8) and (14) gives

$$\Psi \sim \frac{F_{driving}}{F_F} \sim \frac{\Delta P}{\mu E_p} \frac{r_p {r_w}^2}{H_p \Delta A_{pw}} \qquad (15)$$

In the shape mismatched case (**Fig. S11c, d**), there are gaps ($\sum_i \Delta A_{wpi} = \Delta A_{wp}$) between microparticles and microwells. Thus, forces assembling particles into microwells are originated from the pressure difference (F_P) and shear stress (F_s) associated with fluid flow through these gaps (ΔA_{wpi}). Estimating the ratio of resistance of these gaps (R_{wp}) to membrane (R_m) gives the ratio of pressure differences; volumetric flow through the gaps and membrane must be same.

$$\frac{P_1-P_2}{P_2-P_3}=\frac{R_{wp}}{R_m} \tag{16}$$

Hydrodynamic resistance of parallel circular channels is calculated as

$$R_{circular}\sim\frac{\eta L}{\sum_i {A_i}^2} \tag{17}$$

where η is the viscosity of solution, L is the length of the channel, and A_i is the cross section area of each channel. Note that R_{wp} and R_m consist of parallel gaps and pores. The cross sections of gaps are distinctive to each other but can be assumed to be close to the circle. Substituting Eq. (17) into Eq. (16) gives the ratio of pressure differences, which is defined as C.

$$C\sim\frac{P_1-P_2}{P_2-P_3}\sim\frac{D_{pore}H_p {A_{pore}}^2}{H_{pore}\sum{\Delta A_{wpi}}^2} \tag{18}$$

where H_{pore} is the height of pore, D_{pore} is the number of pores inside a microwell, and A_{pore} is the cross section area of pore. When particles have not extreme, but distinctive shape difference from each other, $A_{pore}\ll\Delta A_{wp}\ll\pi {r_w}^2$, resulting in $\mathrm{C}\ll 1$. Combining Eqs. (3) and (18) gives

$$P_1-P_2=C\Delta P \tag{19}$$

Once the particle is assembled into the microwell in shape mismatched case, the cross section area which affects by pressure difference becomes

$$\pi\bar{r}^2=\pi {r_w}^2-\Delta A_{wp}\cong\ \pi {r_w}^2 \tag{20}$$

Substituting Eqs. (19) and (20) into Eq. (1) gives

$$F_P\sim C\Delta P {r_w}^2 \tag{21}$$

The velocity of flow through each gap (v_{wpi}) and the corresponding shear stress on the particle (σ_{wpi}) are

$$v_{wpi} \sim \frac{P_1 - P_2}{\Delta A_{wpi} R_{wpi}} \sim \frac{C \Delta P \Delta A_{wpi}}{\eta H_p} \tag{22}$$

$$\sigma_{wpi} \sim \eta \frac{v_{wpi}}{\sqrt{\Delta A_{wpi}}} \sim \frac{C \Delta P \sqrt{\Delta A_{wpi}}}{H_p} \tag{23}$$

The force generated by shear stress on the particle is

$$F_S \sim \sum_i (\sigma_i \sqrt{\Delta A_{wpi}} H_P) \sim C \Delta P \sum_i \Delta A_{wpi} = C \Delta P \Delta A_{wp} \tag{24}$$

Comparing Eqs. (21) and (24), $F_P \gg F_S$ because $\pi {r_W}^2 \gg \Delta A_{WP}$. Thus, in the shape mismatched case, the driving force is

$$F_{driving} = F_P + F_S \cong F_P \sim C \Delta P {r_w}^2 \tag{25}$$

Eq. (14) is the general equation of friction force which is valid in both shape matched and mismatched cases. Combining Eqs. (14) and (25) gives

$$\Psi_{mis} \sim \frac{F_{driving}}{F_F} \sim \frac{D_{pore} H_p {A_{pore}}^2}{H_{pore} \sum {\Delta A_{wpi}}^2} \frac{\Delta P}{\mu E_P} \frac{r_P {r_W}^2}{H_p \Delta A_{pw}} \sim \mathrm{C} \Psi \tag{29}$$

ΔA_{pwi} and ΔA_{wpi} vary depending on how particle and microwell are overlapped. As a representative value, it is reasonable to use the case when the centers of mass of the cross section of particle and microwell are matched.

Measurement of microparticles' modulus

Modulus of microparticles is required to estimate dimensionless numbers (Ψ, Ψ_{mis}) of assembly processes. Modulus of microparticles has been measured by using atomic force microscopy (AFM)[5, 6], capillary micromechanics[3, 4], and bulk measurements[4]. The result of AFM measurement represents only surface characteristics, and it is hard for 2D extruded structure to use capillary micromechanics. Although bulk measurement is the most convenient method, it is hard to claim that it represents the value of microparticles. To solve this problem, here, we show the analytical approach to mimic the microparticles' condition in bulk scale. The most critical aspects affect the modulus are prepolymer composition and degree of polymerization. Prof. Doyle group developed the model for degree of polymerization of microparticle synthesized via SFL in 2008[7]. Two governing equation is given as

$$\frac{\partial\theta}{\partial\tau} = \frac{\partial^2\theta}{\partial\eta^2} - Da \tag{30}$$

$$-\int_1^{\xi} \frac{\partial\xi}{\xi} = \int_1^{\tau} \frac{Da'}{2\theta} d\tau \tag{31}$$

where θ is a dimensionless oxygen concentration in the prepolymer solution, τ is a dimensionless time, η is a dimensionless z position (along the height), ξ is a dimensionless monomer concentration, and Da, Da' are Damköhler numbers.

$$\theta = [O_2]/[O_{2,eqb}] \tag{32}$$

$$\tau = \mathrm{t}D_O/H^2 \tag{33}$$

$$\eta = \mathrm{z/H} \tag{34}$$

$$\xi = [\mathrm{M}]/[M_0] \tag{35}$$

$$\mathrm{Da} = \frac{\varphi I\varepsilon[PI]H^2}{[O_{2,eqb}]D_O} \tag{36}$$

$$\mathrm{Da}' = \frac{2\varphi I\varepsilon[PI]H^2 k_p}{[O_{2,eqb}]D_O k_O} \tag{37}$$

where $[O_2]$ is the oxygen concentration in the prepolymer, $[O_{2,eqb}]$ is the equilibrium concentration of oxygen in the prepolymer, t is curing time, D_O is the diffusivity of oxygen in the prepolymer, H is the height of channel, z is the height of location (z = 0 at the bottom of channel), [M] is the monomer concentration, $[M_0]$ is the initial monomer concentration, φ is the quantum yield of radical formation, I is the light intensity, ε is the molar extinction coefficient of the photoinitiator, k_p is the rate constant of propagation step, and k_O is the rate constant of oxygen inhibition process.

When two prepolymer solutions are prepared identically and share same dimensionless numbers, it is possible to claim that two prepolymer solutions have the same degree of polymerization. In order to match all dimensionless numbers of two systems which have different length scale, two requirements should be satisfied.

$$I_1 {H_1}^2 = I_2 {H_2}^2 \tag{38}$$

$$\frac{t_1}{{H_1}^2} = \frac{t_2}{{H_2}^2} \tag{39}$$

Each subscript number represents the system (1: microscale, 2: bulk scale). Based on this analysis, bulk microparticle, which mimic the microparticle's modulus, was synthesized in PDMS well (**Fig. S14a**), which is corresponding to the PDMS microfluidic channel. Compressive modulus was measured by rheometer (TA instruments, AR-G2) (**Fig. S14b**)[4]. Gap between two plates represents the height of the particle, and axial force is divided by top area of particle to calculate the stress (**Fig. S14c**). At the beginning, slightly curved microparicles tends to be flat, and axial force is not accurately measured due to the additional force to make particle flat. Therefore, data was obtained after particle becomes perfectly flat. Initial height is extrapolated by assuming axial force is zero at initial state. Then, the compressive modulus is estimated by finding the slope of strain-stress curve (**Fig. S14d**).

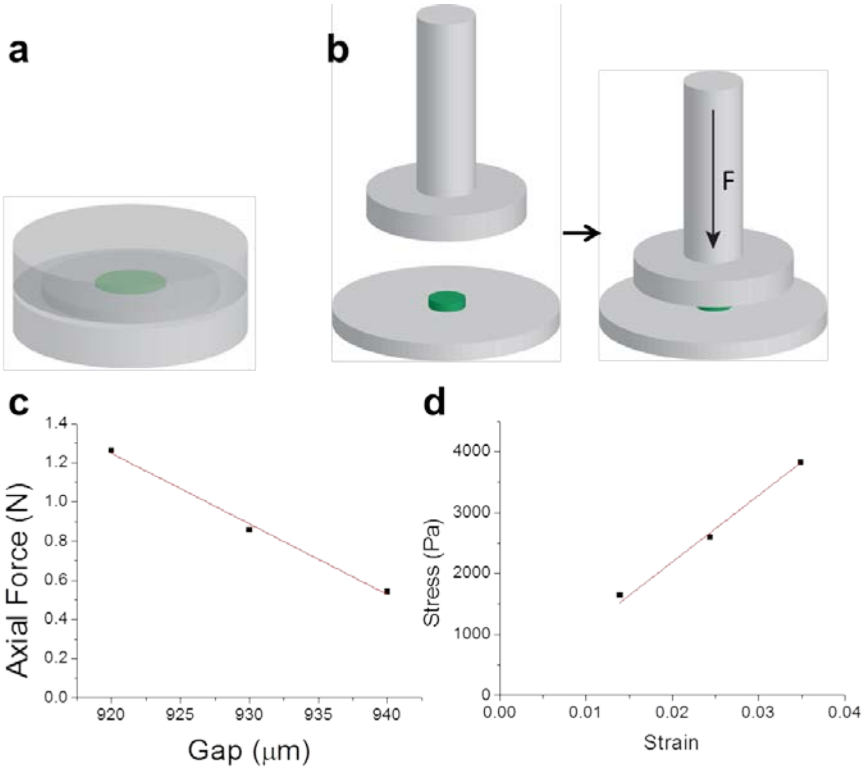

Figure S14. Bulk measurement of microparticles' modulus. a, Schematic for the fabrication of bulk particle which mimics the modulus of microparticle. **b**, Schematic for bulk measurement of compressive modulus. **c**, Plot for axial force versus measured particle height (gap between two plates). Plotted data is for 35 % PEGDA particles. **d**, Strain-stress curve for compressive modulus calculation. Slope of the plot represents compressive modulus.

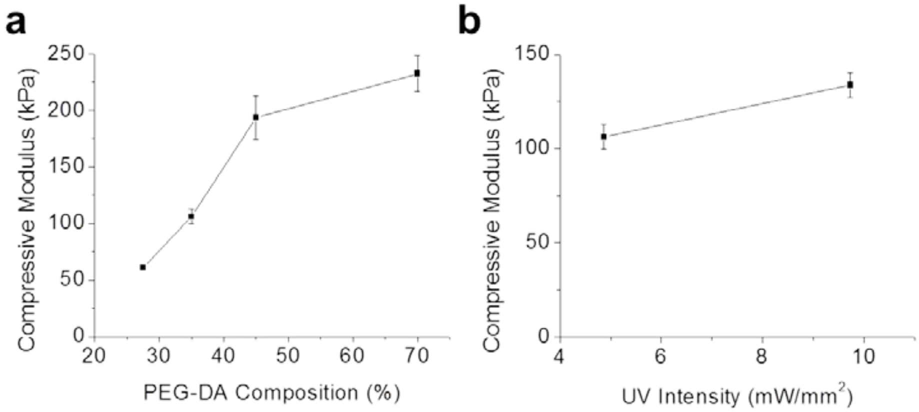

Figure S15. Measured compressive modulus of particles. **a**, Compressive modulus as a function of composition of prepolymer solution. Large particle mimic the condition of microparticles polymerized under the UV exposure (365 nm, 4.87 mW/mm^2). **b**, Compressive modulus as a function of UV intensity. Prepolymer solution consists of 35 % PEG-DA composition. Higher PEGDA composition and UV intensity increase compressive modulus of microparticles. Error bars represent standard deviation (n = 3, 4).

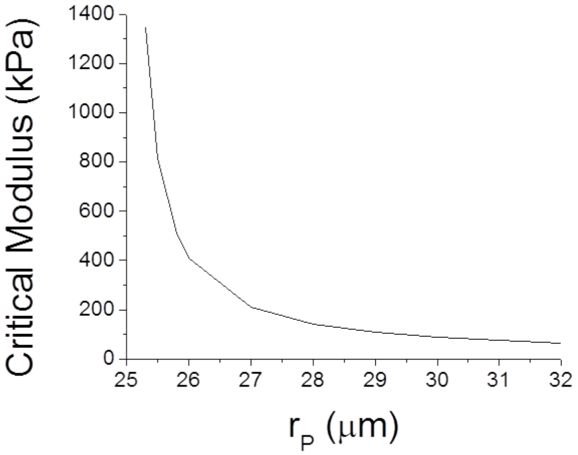

Figure S16. The relationship between particle size and modulus. Particles which have the characteristics only under the trend line can fit into microwells; particles in the upper region cannot fit into microwells. As r_P decreases, more rigid particle (with higher E_p) can fit into microwells. This plot is made in the case that both particle and microwell have the cylindrical shape, and r_w(= 25 μm), H_p (= 35 μm), μ (~10^{-3}), and ΔP (=54 Pa) remain constant.

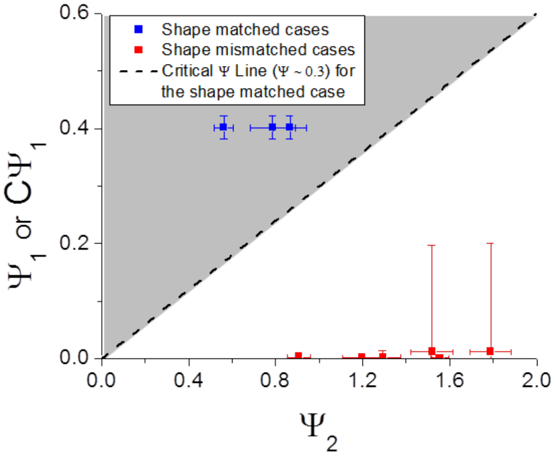

Figure S17. Scaling analysis for shape specific positioning. Phase diagram, Ψ_1(shape-matched) or $C_1\Psi_1$(shape-mismatched) as a function of Ψ_2, for particle assembly in **Fig. 2i**. Small value of C ensures the high shape specificity. For all shape mismatched cases in **Fig. 2i**, the assumption ($A_{pore} \ll \Delta A_{wp} \ll r_w$) to simplify the dimensionless number is valid. Error bars represent standard deviation (n = 3, 4).

Spherical particle assembly

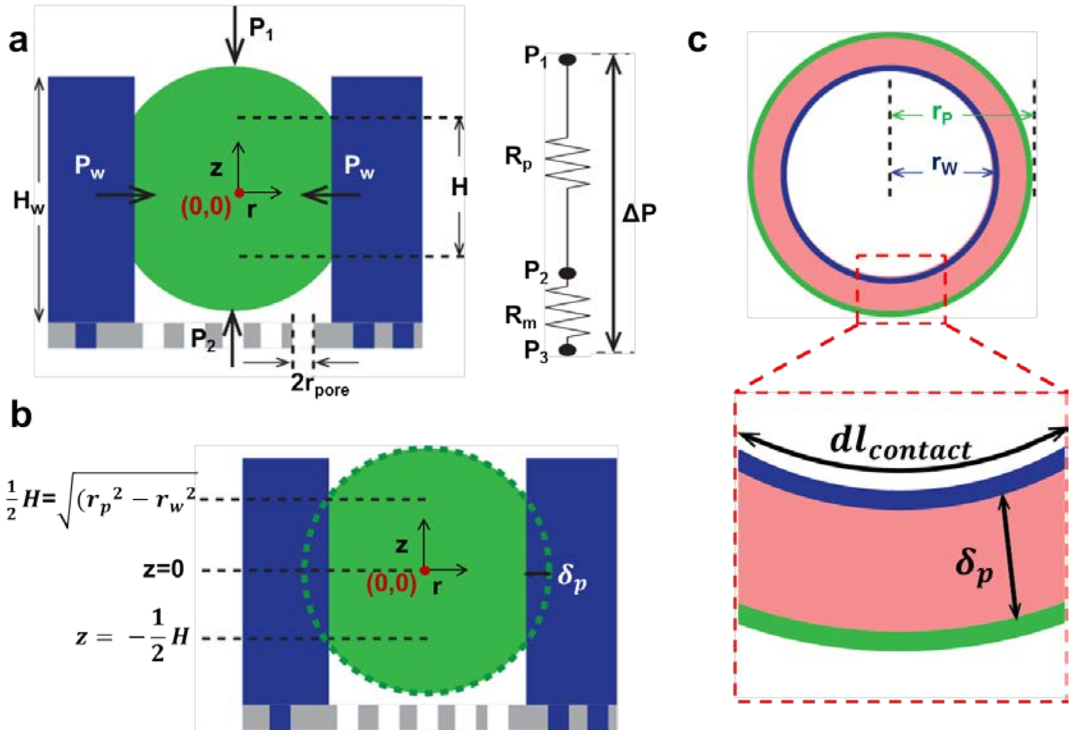

Figure S18. Schematics of scaling analysis for spherical microparticle assembly. a, Side view. **b,** Side view for particle deformation (δ_P) over the contact height (H). Green dotted line represents original particle shape. **c,** Top view.

As assumed previously, a microwell does not deform during the particle assembly process. Consider two forces acting on the microparticle (**Fig. S18**): 1. Assembly force originated from pressure difference across the particle (F_p). 2. Friction between the particle and the wall of microwell (F_F). As justified previously, consider only the point where the ratio of F_P to F_F is minimized. Therefore, we consider the point which particles were deformed in a maximum level as shown in Figure S18a. Because there is no gap between particle and microwell, assembly force (F_p) becomes same as Eq. (8) in the shape matched case.

$$F_P \sim \Delta P \, {r_w}^2 \tag{8}$$

As did, based on the interference fit[2] and capillary micromechanics[3, 4], F_F is scaled as

$$F_F \sim \int \mu P_w \, dA_{contact} \tag{40}$$

Wall pressure (P_w) is originated from particle deformation (δ_p), and P_w is scaled as Eq. (9).

$$P_w \sim \frac{E_p \delta_p}{r_p(1-\nu_p)} \sim \frac{E_p \delta_p}{r_p} \tag{9}$$

In spherical microparticle assembly, δ_p varies along the z-direction (**Fig. S18b**).

$$\delta_p = \sqrt{{r_p}^2 - z^2} - r_w \tag{41}$$

$l_{contact}$ ($= 2\pi r_w$) is constant for spherical particle assembly (Fig. SS6.c). Substituting Eqs. (9) and (41) into Eq. (40) gives

$$F_F \sim \int \mu P_w \, dA_{contact} \sim 2 \int_0^{\sqrt{{r_p}^2 - {r_w}^2}} \mu \frac{E_p}{r_p} \left(\sqrt{{r_p}^2 - z^2} - r_w\right) 2\pi r_w dz \tag{42}$$

Integrating Eq. (42) gives

$$F_F \sim \frac{2\pi\mu E_p r_w}{r_p} \left[{r_p}^2 \tan^{-1}\left(\frac{\sqrt{{r_p}^2 - {r_w}^2}}{r_w} \right) - r_w \sqrt{{r_p}^2 - {r_w}^2} \right] \tag{43}$$

Dimensionless number ($\Psi_{spherical}$) is given by combining Eqs. (8) and (43).

$$\Psi_{spherical} \sim \frac{F_{driving}}{F_F} \sim \frac{\Delta P \, r_w r_p}{2\pi\mu E_p} \left[{r_p}^2 \tan^{-1}\left(\frac{\sqrt{{r_p}^2 - {r_w}^2}}{r_w} \right) - r_w \sqrt{{r_p}^2 - {r_w}^2} \right]^{-1} \tag{44}$$

To demonstrate sorting of spherical particles, new experiments were performed. Various sized, spherical PEGDA microparticles were sorted with porous microwell arrays (**Fig. S19**). Microparticles were made by following procedure. 3 µl of 70 % PEGDA prepolymer solution was added into 600 µl mineral oil (Sigma Aldrich), vortexed for 5 seconds, and cured by UV lamp for 4.5 minutes. Synthesized microparticles were purified with DI water and ethanol, and stored in 1× TET solution (**Fig. S19a**). When microparticles were assembled into 26.5 µm microwells, only particles, which have similar diameters to microwells, can fit into microwells, whereas larger microparticles were removed during the washing step (**Fig. S19b**). By assuming these microparticles have same elastic modulus with 70 % PEGDA microparticle synthesized via SFL (spherical microparticle might have higher modulus than SFL microparticle because there is no oxygen inhibition layer, and they were synthesized for a longer exposure time), $\Psi_{spherical}$ vs. r_p can be plotted as Figure S20.

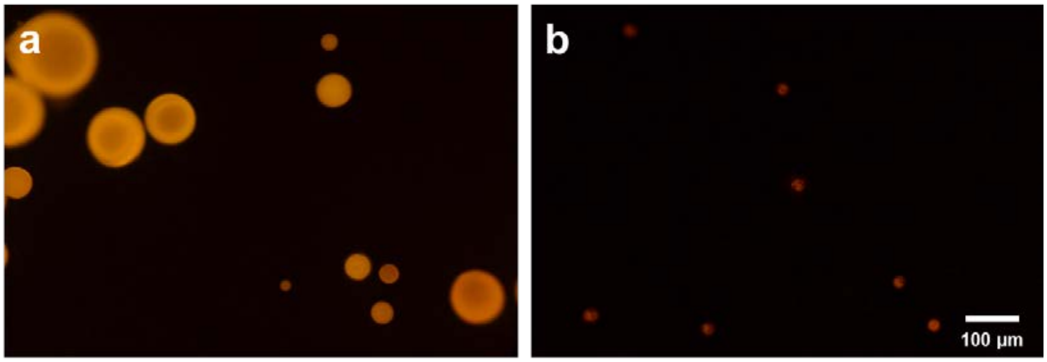

Figure S19. Spherical microparticle sorting. a, Spherical PEGDA microparticles with various sizes. **b,** Result of size-specific sorting with spherical microparticles.

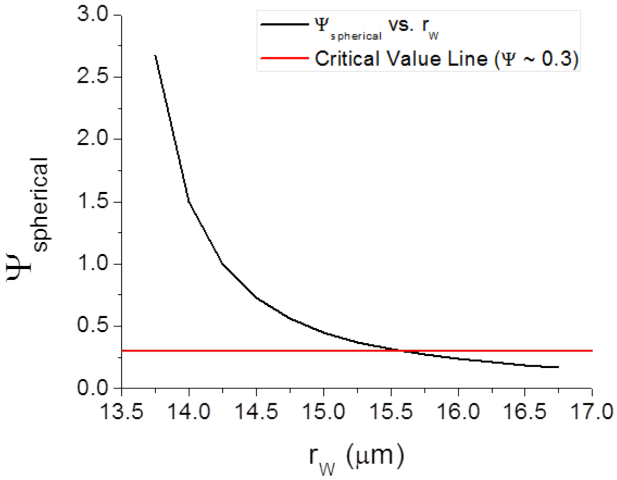

Figure S20. $\boldsymbol{\Psi_{spherical}}$ vs. $\boldsymbol{r_p}$ plot. Black line represents calculated $\Psi_{spherical}$ corresponding to r_p. The critical value line is drawn as the red line by assuming spherical particle has same critical value as the shape matched case. Particles below this red line are unable to be assembled. In our experiment, the microwell's diameter is fixed as 26.5 μm. Particles with diameters larger than 31 μm cannot be assembled into microwells.

Brownian colloids assembly

Consider the case of Brownian colloids, which are generally considered as particles smaller than 2 µm. Driving force of our platform acts on microparticles during two processes: 1) guiding particles to microwells and 2) particle assembly into microwells. The particle assembly process can be described by a dimensionless number (Ψ). Our goal is understanding the difference between large and small length scales, so we can solely focus on the geometrical factor (Ψ_2). When calculating Ψ_2, the important value is the relative ratio of r_p to r_w, not absolute value of r_p or r_w. Therefore, we can conclude that there will be no significant difference in the assembly process between Brownian and non-Brownian particles.

On the other hand, there is an interesting difference in the guiding process. Fluid flow advects colloids and there is also Brownian motion. Brownian colloids can be effectively guided to microwells when advective motion overcomes Brownian motion (**Fig. S21**). This can be described by a flux balance.

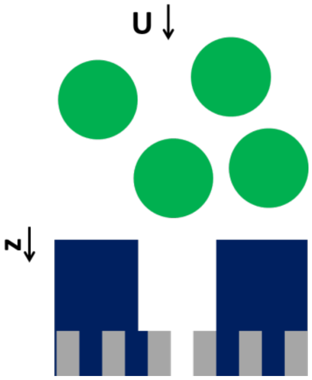

Figure S21. A schematic for scaling analysis of guiding Brownian colloids into microwells. Green sphere represents Brownian colloids.

$$N_c = -D_c \frac{\partial C_c}{\partial z} + UC_c \tag{45}$$

N_c is flux of colloids toward z direction, D_c is the diffusivity of colloids, C_c is the concentration of colloids, and U is the convective velocity of colloids, which is scaled as flow rate.

Concentration of colloids is scaled as

$$C_c \sim C_{c,bulk} e^{(\frac{zU}{D_c})} \tag{46}$$

$C_{c,bulk}$ is the bulk concentration of colloids. Therefore, particles which are located in the range of D_c/U from the PET membrane, can be effectively assembled into a microwell. This effective length should be longer than the microwell height in order to guide microparticles outside the microwell. Considering that the microwell height is scaled as the diameter of colloids, we can find the dimensionless number governing the guiding process: the Péclet number (Pe). Using the Stokes-Einstein relation,

$$\text{Pe} \sim \frac{Ur_c}{D_c} \sim \frac{\eta {r_c}^2 U}{kT} \tag{47}$$

r_c is the radius of colloids, η is the viscosity of solution, k is Boltzmann constant, and T is the absolute temperature. As shown in Figure S22, Brownian colloids can be guided into microwells when Pe is larger than 1.

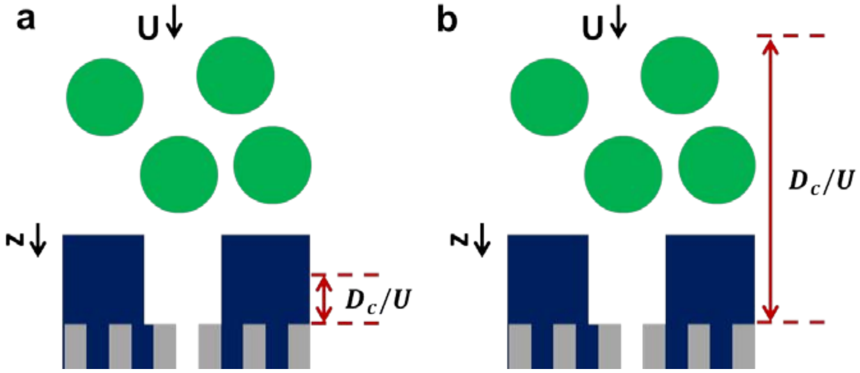

Figure S22. The Criteria of effective guiding. a, Pe < 1; Brownian colloids cannot be guided into microwells. **b,** Pe > 1; Brownian colloids can be guided into microwells.

As ΔP increases, we can increase U, resulting in higher Pe and better guiding. At room temperature, U is required to be higher than 1×10^{-5} m/s in order to effectively guide particles with 1 µm diameter. By assuming that there is one pore with d_{pore} = 0.5 µm inside a microwell ($H_w \sim r_w \sim r_c$), we can calculate required ΔP.

$$\Delta \mathrm{P} \sim \frac{\eta L_{pore} Q}{{d_{pore}}^4} \sim \frac{\eta L_{pore} U {r_c}^2}{{d_{pore}}^4} \sim 0.7 \text{ Pa} \tag{48}$$

L_{pore} is the length of pore which is about 10 µm for all commercially available PET membrane shown in Figure S4. Q is the volumetric flow rate. Practically, the ΔP calculated in Eq. 48 can be easily achieved. Moreover, as ΔP increases, the efficiency of guiding will increases further.

In previous microwell based approach[5], there is no controllable driving force, and only gravity is used for particle guiding and assembly. In this case, U is given as a fixed value, sedimentation velocity.

$$U_{gravity} \sim \frac{\Delta\rho g {r_c}^2}{\eta} \tag{49}$$

$\Delta\rho$ is the density difference between colloids and solvent, g is the gravity acceleration. Therefore, concentration of colloids and Pe are scaled as

$$C_c \sim C_{c,bulk} e^{\left(\frac{z U_{graviity}}{D_c}\right)} \tag{50}$$

$$Pe_{gravity} \sim \frac{U_{gravity} d_c}{D_c} \sim \frac{\Delta\rho g {r_c}^4}{kT} \tag{51}$$

For colloids with 1 µm diameter and 0.05 g/cm^3 density difference (e.g. polystyrene bead), $Pe_{gravity}$ equals 0.01. Therefore, with only gravity, it is much harder to guide Brownian colloids to the assembly template (microwells) compared to our platform. In conclusion, compared to prior work using sedimentation, our platform is more suitable to guide and assemble Brownian colloids.

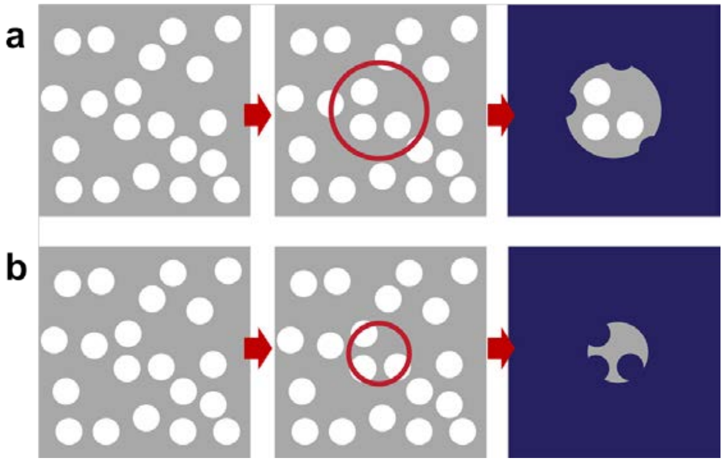

Figure S23. Importance of relative size of microwell to pore of porous membrane. a, Microwell is larger than pores. **b,** Microwell size is close to the pore size. Left images show the porous PET membrane. Red circle of middle images represents the location of a microwell. Right images show the fabricated porous microwells. White and blue pore represent open and close pore, respectively.

We now consider the technical issues of making small porous microwells. Figure S22.b describes the case when the microwell size is close to the pore size. In this case, pore is hard to be perfectly inside of the microwell. When pore size is fixed and the microwell size decreases it becomes statistically less likely to have at least one open pore inside a microwell. Figure S8, 9, 23shows assembly of microparticles smaller than 30 µm (**Fig. 1h**). Microparticles were assembled with a vacuum system (**Fig. S2k**). With porous PET membrane (d = 3.0 µm, Millipore, **Fig. S4e**), 20 µm microparticle assembly were successfully demonstrated with a high yield (76 %, **Fig. S9**). As particle and microwell size decrease to 15 µm, the yield of assembly decreases significantly (34 %, **Fig. S24**). However, this limitation comes from the manufacturing specifications of the porous membrane, not the design of our platform. To support this claim, 15 µm particle assembly was demonstrated with a different porous membrane (d = 1.0 µm, Greiner bio-one, **Fig. S4c**). As can be seen in Figure S10, the yield of assembly increases to 49 %. This improvement is because the pore (d = 1.0 µm) is more likely to be open inside of a microwell (d = 15 µm). If the following three requirements of the porous membrane are satisfied, it will be possible to assembly much smaller particles: 1. The location of pore in membrane is precisely predefined. 2. The pore size of membrane is slightly smaller than microwell size. 3. Microwell mold is placed on top of membrane while mold is precisely aligned with pores of membrane. Another possible solution will be replacing porous PET membrane with other porous materials (e.g. porous graphene-based bulk materials[6, 7]) in order to achieve small particle assembly without concern of the alignment of pore with microwell.

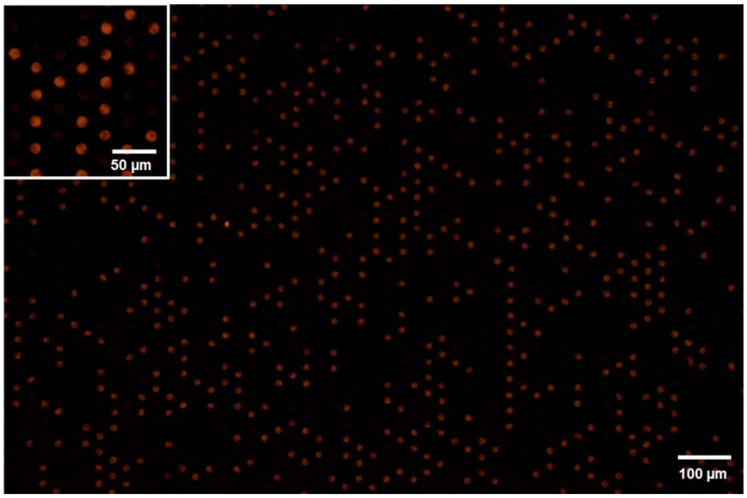

Figure S24. 15 µm particle assembly. ~ 34 % of microwells were filled with microparticles. Microwell arrays were made with porous PET membrane (d = 3.0 µm, Millipore, **Fig. S4e**). Height of microwell (H_w) and particle (H_p) are 15 µm.

Uniform pressure over the array

There is no direct way to measure the suction pressure of each microwell. Here, we describe the rationale for homogeneous suction pressure distribution over a large area. Over both narrow (16 mm^2) and wide (64 mm^2) areas, particle sorting was successfully demonstrated with a high specificity and a narrow deviation (**Fig. S25**) If there is high polydispersity of suction pressure over the area, particle sorting is not achievable with high specificity. We measured the flow rate through the microwell array over a narrow and wide area (**Fig. S26**). By varying the area of exposed microwells and maintaining the liquid height, we can check how homogeneous the suction pressure is. Regardless of area, the same height of liquid takes same time to pass through the membrane. Therefore, we can infer that suction pressure is homogeneous over the large area, ensuring the scalability of this approach.

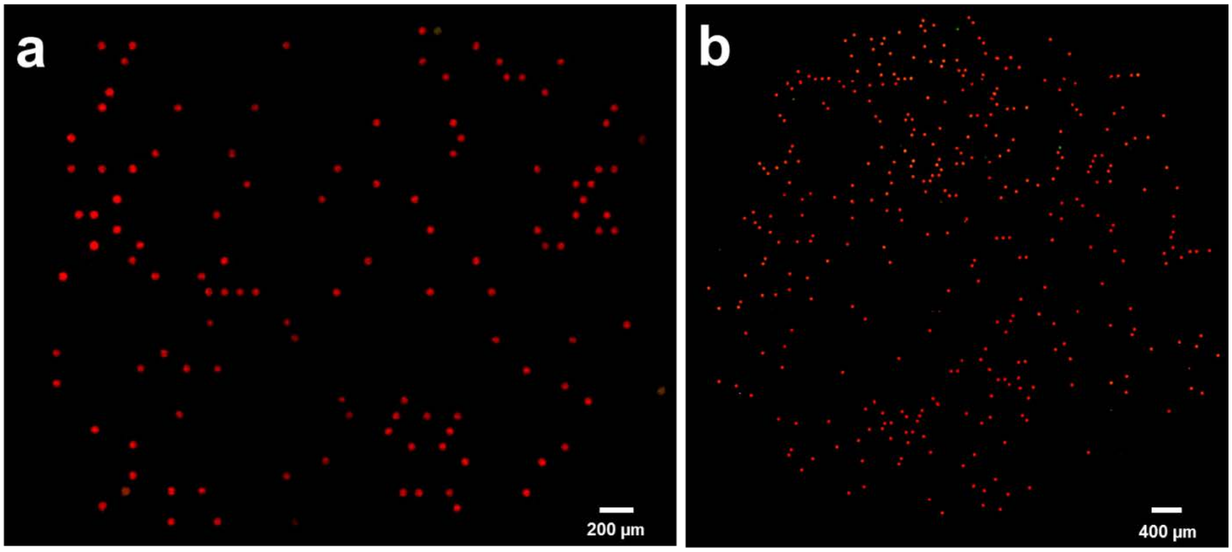

Figure S25. Modulus sorting results over 16 mm^2 (a) and 64 mm^2 (b). Specificity of each result was 96.49 % (a) and 95.98 % (b), respectively.

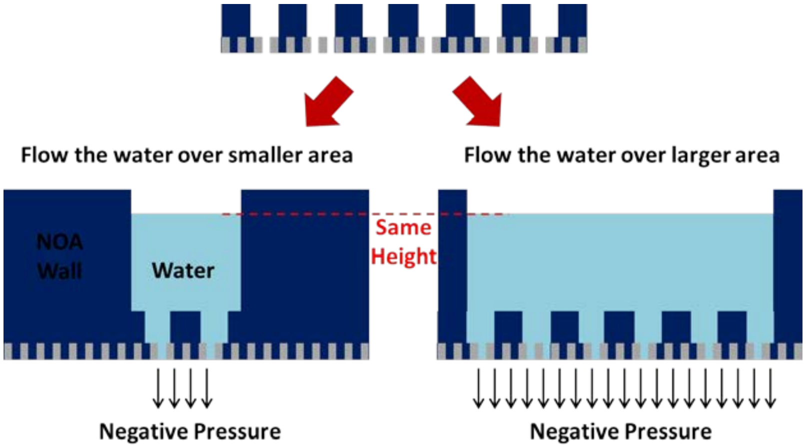

Figure S26. Comparison of suction pressure between small and large area.

Diameter of NOA wall	Added water volume	Flow time
4 mm	20 µL	~ 4 seconds
8 mm	80 µL	~ 4 seconds

Table S3. Results of suction pressure comparison.

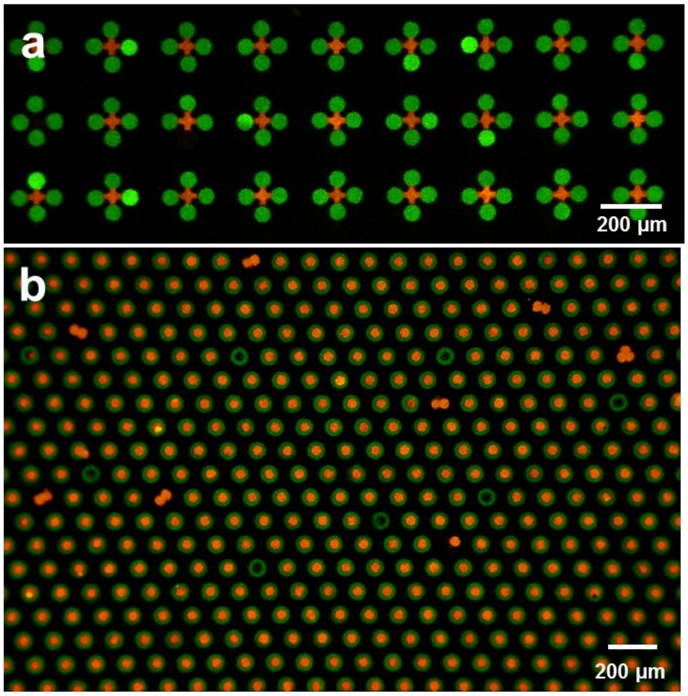

Figure S27. Sequential assembly at proximal locations in larger view. Particles are located next to each other (**a,** success rate = 75.9 % = (93.3 %)^5), or inside the hole of another particle (**b,** success rate = 96.8 % = (98.4 %)^2).

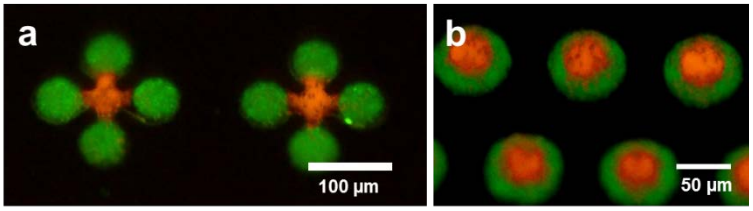

Figure S28. Images of ~20° tilted microwell arrays for sequential assembly. Particles are located next to each other (**a**), or inside the hole of another particle (**b**). ~20° angled PDMS support is placed under the microwell arrays. Multiple particles in a single microwell were sitting leveled.

Cell Culture and Live Staining. Single cell array experiments were performed using adherent glioma U87 cell line (ATTC, Manassas, VA). Cells were cultured in DMEM Medium supplemented with 10 % (v/v) FBS and 1 % (v/v) pen/strep, at 37°C and 5 % CO_2 until cells were 70 to 80 % confluent. One hour before the experiment, cells were thoroughly washed with PBS and then stained using a fluorescence cell tracker green CMFDA dye (Life Technologies, Woburn, MA, USA). The dye was prepared according to the manufacturer's instructions and was supplied to the cells in serum free media at a concentration of 0.5 µM. U87 cells were incubated with the dye at 37°C and 5 % CO_2 for 15 min. Excess dye was removed by washing the cells three times with PBS while there were attached to a flask. Subsequently, stained cells were incubated in 2 mL of 0.025 % (v/v) trypsin for cell detachment. Cells were centrifuged at 1000 RPM for 5 minutes and resuspended in cell culture media at a concentration of 1x10^6 cells/ml.

Single cell assembly. NOA 81 microwell arrays (diameter ~ 25 µm) were fabricated by following the protocol in the main text (**Fig. S1, S2**). Microwell arrays were confined by PDMS wall (diameter = 8 mm), and 50 µl of PBS and 100-150 µl of cell suspension were dispensed on microwell arrays. Cells were assembled into microwells with a Kimwipe (capillary wetting) driving the flow, and microwell arrays were gently washed with DMEM media. Over the process, cells should not be dried.

Scanning Electron Microscopy (SEM) Sample Preparation. Patterned U87 cells in microwells were chemically fixed overnight with 2 % glutaraldehyde in 0.1 M sodium cacodylate. Samples were washed with 0.1 % sodium cacodylate, and then they were gradually dehydrated in different volume percentages of ethanol (50 %, 70 %, 80 %, 95 %, and 100 %) for 15 minutes incubation steps. Samples were transferred to a CO_2 critical point drier Autosamdri 931 (Tousimins, Rockville, MD, USA). Dried samples were sputtered with a Platinum/Palladium target at a rate of 10 A°/min for a thickness of 10 nm. Scanning electron microscopy (SEM) was performed in a Supra FV500 (Zeiss, Peabody, MA, USA). Samples were imaged at different magnifications using an accelerating voltage of 3 kV.

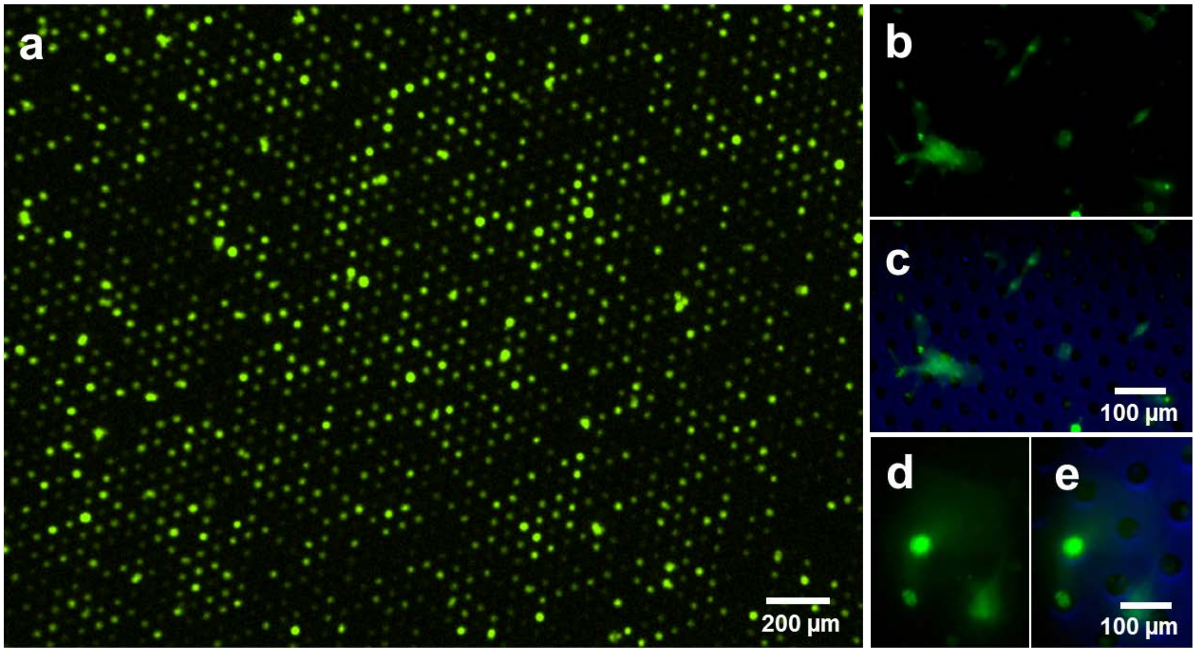

Figure S29. Single cell arrays. a, Approximately 10,000 cells are arranged in 15000 microwells on a 50 mm^2 surface area. The microwells contain either one or no cells. **b-e**, Cell viability and spreading. 4.5 days after assembly, assembled cells are attached and spreading over the surface of the microwells. **b**, **d** show only fluorescence images of the cells, and **c**, **e** show the overlapped images of cells and microwells. **d**, **e** show the spreading of squeezed cells into microwells.

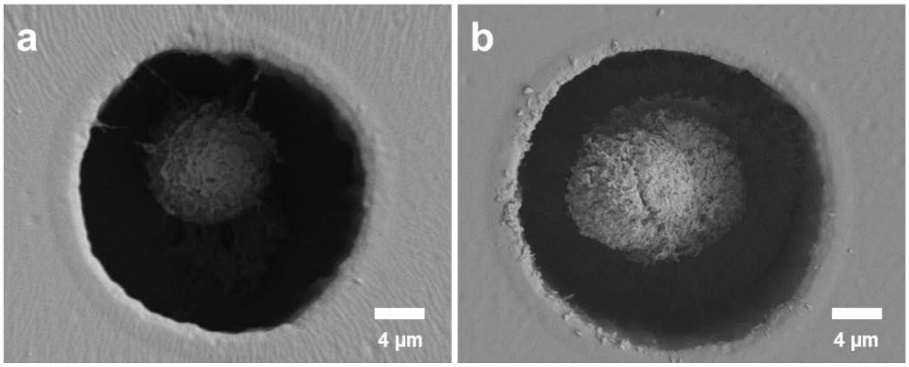

Figure S30. Scanning electron micrographs of individual cells inside microwells. The diameter and depth of the wells match the diameter of the cells such that only one cell fits inside a well at a time.

Chemoattractant-loaded microparticle fabrication. 35 % PEGDA microparticles (d ~ 100 µm) and 94 % PEGDA microparticles (d ~ 60 µm) were synthesized and stored in PBST (PBS buffer with 0.05% Tween-20). Fluorescent bead (carboxylated, YG) and rhodamine acrylate were incorporated in 35 and 94 % PEGDA particles, respectively. 94 % particles' prepolymer solution was 94 % (v/v) PEGDA 700, 1 % (v/v) 1 mg/ml rhodamine acrylate in PEG 200, and 5 % (v/v) PI. 100 µM LTB4 and IL-8 solution were prepared by diluting ethanol-based stock solution with 94 and 35 % particle solution, respectively. By centrifuging the solution, ~ 5000 particles were concentrated in 15 µl solution. The solutions of concentrated particles were then dried under argon. Dried particles were quickly re-dispersed in PBST solution before being loaded into the LSMA. To assure high yield of loading, the array was set using a 3 µm pore membrane from corning (Fig. S4b) and particles were sequentially loaded into wells assisted by vacuum suction setup (**Fig. S2k**). Particle arrays were gently rinsed with PBST to remove excess particles, dried, and stored in the cold room, ready to use.

Neutrophil Isolation, Staining and Quantification. Human blood from healthy donors was drawn according to an IRB protocol at Massachusetts General Hospital. 10 ml of peripheral blood was collected in heparin tubes (Vacutainer, Becton Dickinson, Woburn, MA, USA) and neutrophils were isolated within two hours after blood collection using EasySep Human Neutrophil Enrichment Kit (STEMCELL Technologies, Vancouver, Canada). After isolation, neutrophils were washed with IMDM media supplemented with 20 % FBS. Neutrophil nuclei were stained with Hoechst 33342 trihydrochloride dye (Life Technologies, Woburn, MA, USA). Stained neutrophils were counted and suspended at 0.5×10^6 cells/ml concentration in cell culture media.

Microparticle arrays were quickly rehydrated and prepared for experiments with cells. Wells (diameter = 8 mm)) in a thick PDMS layer on top of the membrane were designed to accommodate approximately 200 µL of cell suspension was pipetted on microparticle arrays. Glass coverslip (diameter = 12 mm) were placed on top of PDMS wall to close the system. Neutrophils were recorded with time-lapse microscopy imaging at 10x magnification using a fully automated Nikon TiE microscope with an environmental chamber (Micro Device

Instruments, Avon, MA, USA). Images were acquired every 5 seconds. After the experiments were completed, imaging analysis was performed using Elements software (Nikon).

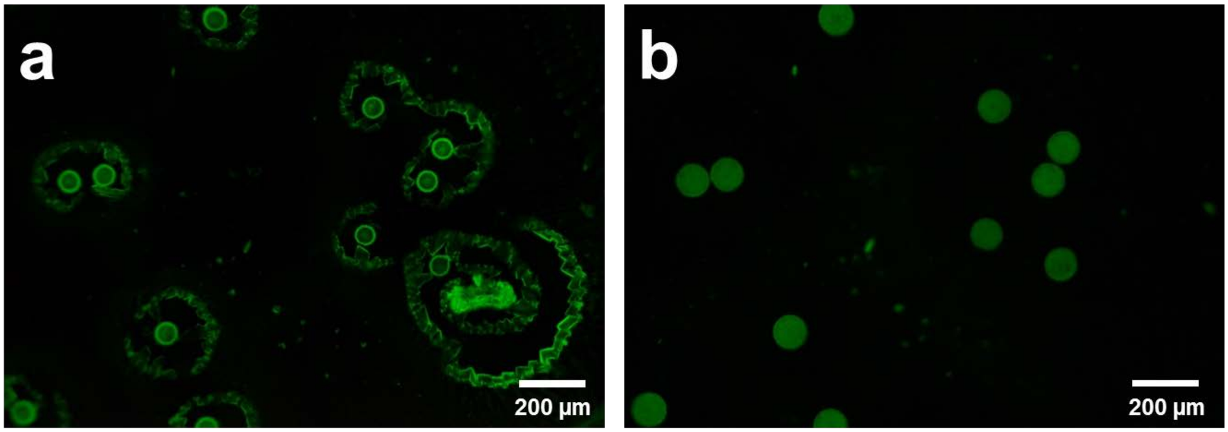

Figure S31. Chemoattractant-laden microparticles for chemical gradient generation. a, Microparticles (35 % PEGDA, d ~ 100 µm) were dispersed in florescent dextran (50k), which has comparable molecular weight with common chemoattractant IL-8, and dried. Because microparticles are hydrophilic, the last portion of evaporated water is around the microparticle. At the end of evaporation, the polymer was concentrated inside microparticles. **b**, Rehydrated chemical-laden microparticles. Chemicals were incorporated homogeneously and remained inside a microparticle for > 20 minutes.

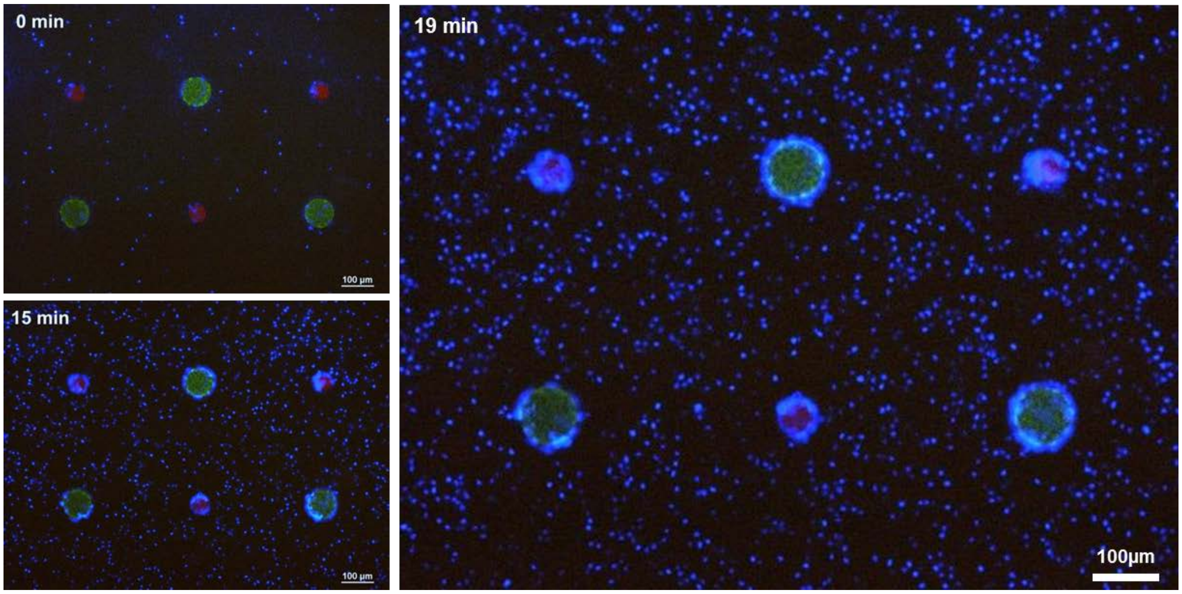

Figure S32. Neutrophil responses to complex chemoattractant gradients, generated by chemoattractant-laden microparticle arrays. LTB4-loaded (red, 60 µm diameter) and IL-8-loaded (green, larger, 100 µm diameter) microparticles are arranged in an alternate pattern. After loading the neutrophils (blue) in a suspension over the LSMA (time 0), neutrophils settle down on the membrane and start migrating on the surface of the membrane.

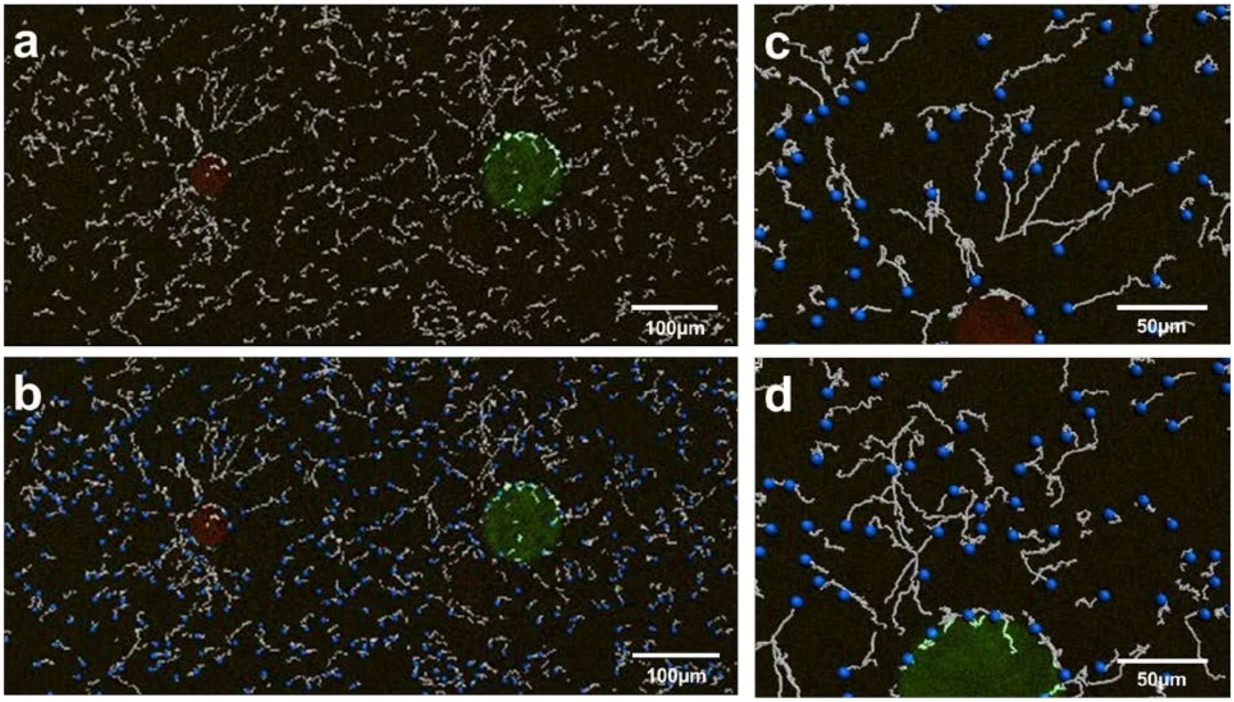

Figure S33. Tracking results of neutrophils migratory responses in complex chemoattractant gradients. Neutrophil tracks for 8 minutes show straight pathways toward the LTB4-laden microparticle (red, small) and more convoluted paths in various directions, around the IL-8-laden particle (green, large). Tracking lines represent 96 time steps (= 8 minutes). **b-d**, Blue dots represent the position of neutrophils at 18 minutes after neutrophil loading to the assay. Together with the white tracks, they indicate the direction of neutrophils migration over time. **c** and **d** show tracking results in close view with a higher resolution.

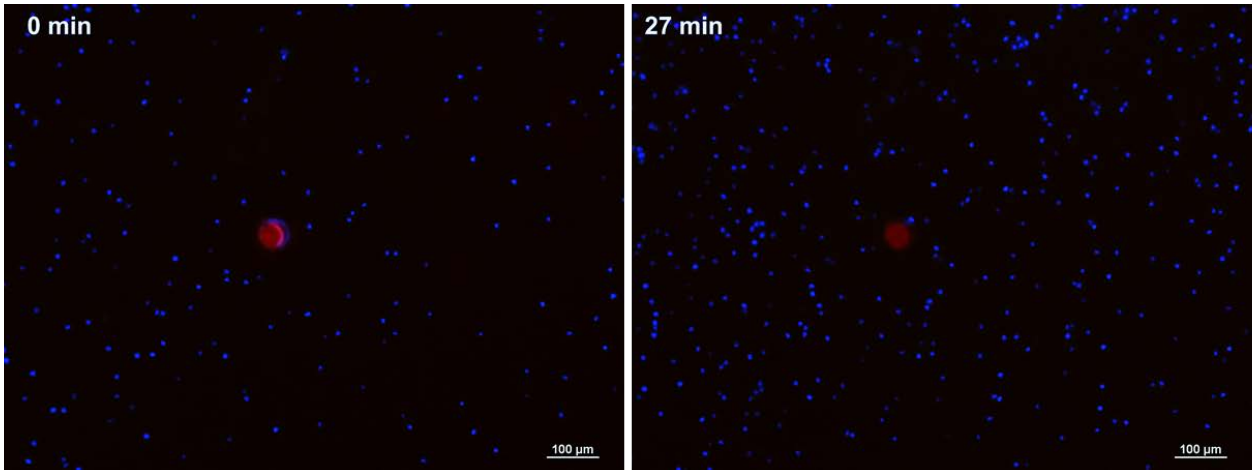

Figure S34. Control experiment for neutrophil migratory response. 35 % PEGDA microparticle (diameter ~ 60 μm, without any chemoattractant) were assembled in an array. Neutrophil migratory responses were observed over 27 minutes. There are no migratory responses toward or away from the particles. The number of neutrophils in the image increases over time due to the sedimentation of neutrophils from the loading suspension.

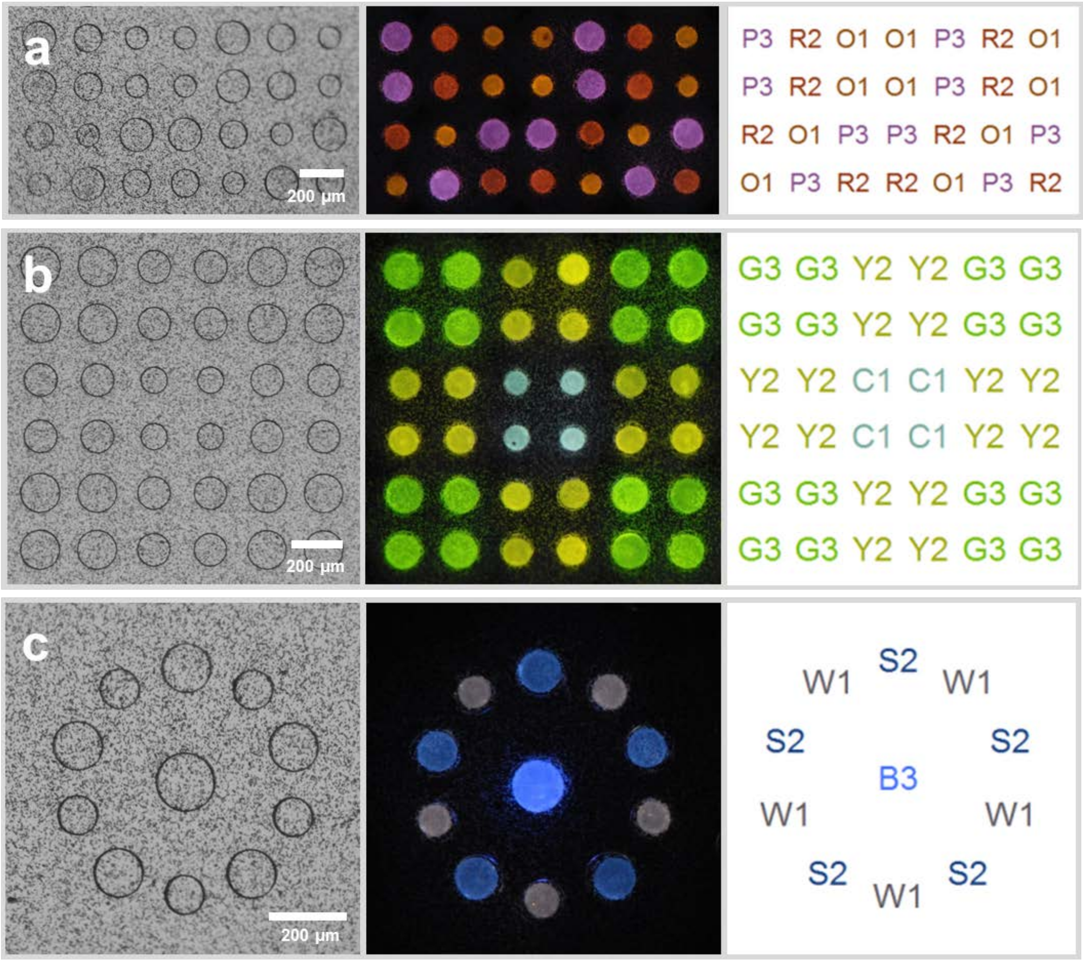

Figure S35. Microparticle arrays for anti-counterfeiting applications. a-c, Sequential assembly and decoding of 2D arranged 6×6 (**a**), 4×7 (**b**), circular (**c**) codes. Each column shows PDMS microwell arrays (left), assembled UCN-laden microparticle array under the NIR exposure (middle), and decoded results in a text form (right). The high modulus of PUA/AA particles ensures no deformation in the assembly process, allowing only microparticles smaller than microwells to be assembled. Shear protection due to the depth of the microwells ensures that microparticles remain inside the well.

UCN-laden microparticle imaging. UCN-laden microparticles in microwell arrays were placed on the stage of inverted microscope (Zeiss, Axiovert 200) and exposed by NIR (Dragon laser, 1W CW 980 nm). NIR laser went through the fiber (Thorlab, diameter = 550 μm) and achromatic doublet pairs (Thorlab). Emitted visible light went through the 5x objective, 980 nm cut-on filter (Semrock Inc.), and Nikon D200. By moving NIR source with xyz stage, several images are taken and overlapped by IamgeJ to get the image of overall arranged particles. After the pattern transfer, target object was placed on the stage of microscope (AmScope, T490A), and transferred particle array was exposed by NIR with ~ 50 ° incident angle. NIR laser went through the fiber (thorlab, diameter = 1500 μm). Overall arranged particle code is exposed by NIR at the same time. Emitted visible light went through the 10x objective (long working distance, NA 0.22), 980 nm cut-on filter, and iphone 5s, which is connected to eyepiece of microscope with adaptor (Magnifi). Image of transferred particle arrays in Figure 5d is shown after adjusting brightness and contrast by ImageJ because when NIR exposes overall particle arrays at the same time, the intensity of NIR becomes weak, resulting in less bright image. However, all images (**Fig. S34**) were decoded without changing brightness and contrast.

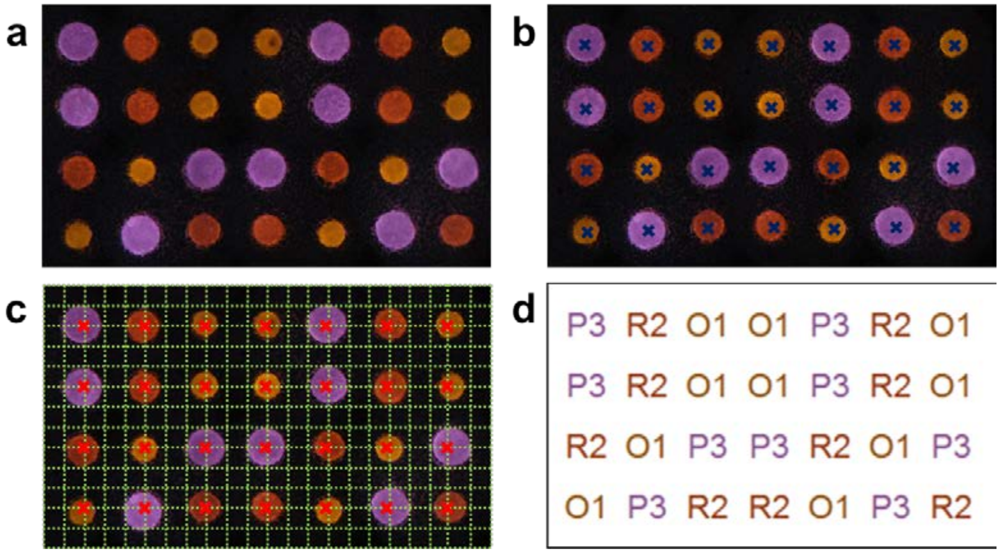

Figure S36. Description of decoding process. a, Input: UCN-laden microparticles in PDMS microwell arrays under the NIR exposure. **b**, Step 1: Detect boundary based on the gray value, find the center (blue marks), and calculate the radius and average color of each particle. Radius and color are compared with standard values. For the image taken by Nikon D200 before the pattern transfer, color is compared with absolute RGB values. For the image taken by iphone 5s after the pattern transfer, relative ratios of color values (R/G, B/G) is used for references (**Table S4**). This is because the image of transferred pattern was taken when NIR exposed all microparticle patterns, resulting varying NIR intensity depending on the position. **c**, Step 2: Make the grid (green dotted lines) and adjust the center location (red marks). The shape of grid is predefined depending on the microparticle pattern. **d**, Step 3: Plot the decoding results.

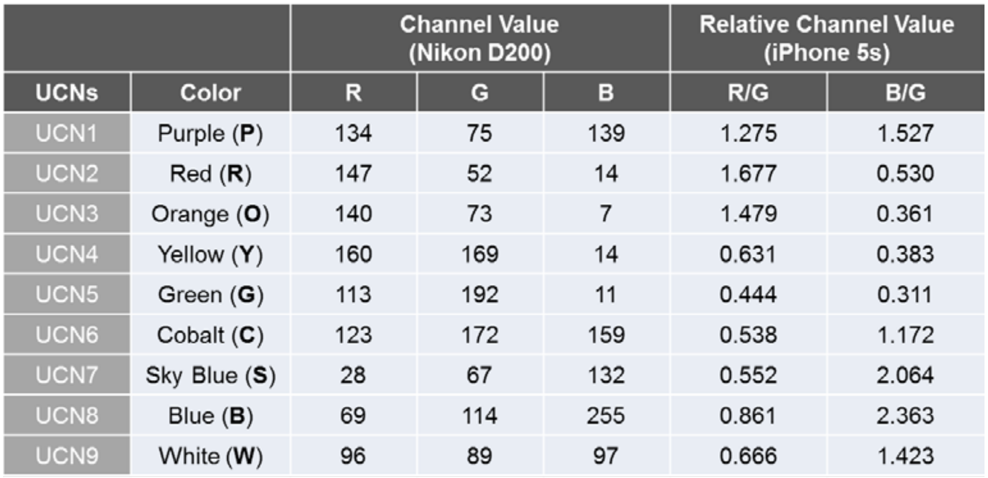

		Channel Value (Nikon D200)			Relative Channel Value (iPhone 5s)	
UCNs	Color	R	G	B	R/G	B/G
UCN1	Purple (**P**)	134	75	139	1.275	1.527
UCN2	Red (**R**)	147	52	14	1.677	0.530
UCN3	Orange (**O**)	140	73	7	1.479	0.361
UCN4	Yellow (**Y**)	160	169	14	0.631	0.383
UCN5	Green (**G**)	113	192	11	0.444	0.311
UCN6	Cobalt (**C**)	123	172	159	0.538	1.172
UCN7	Sky Blue (**S**)	28	67	132	0.552	2.064
UCN8	Blue (**B**)	69	114	255	0.861	2.363
UCN9	White (**W**)	96	89	97	0.666	1.423

Table S4. Standard color values for the decoding process.

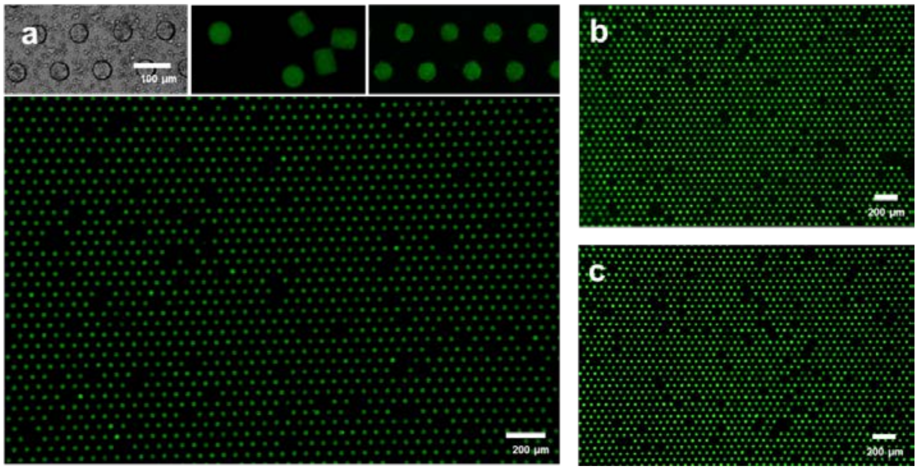

Figure S37. Reproducibility of large-scale, high throughput microparticle assembly. a, Results shown in Fig. 1h. **b, c,** Repeated results.

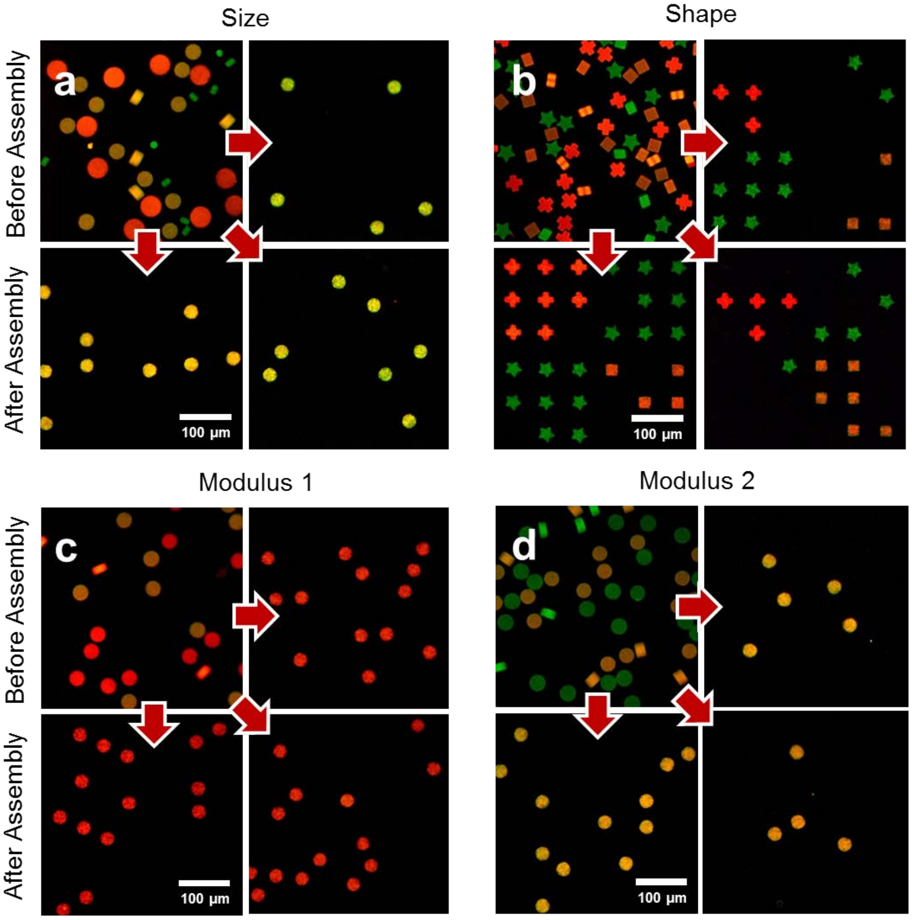

Figure S38. Reproducibility of characteristic specific positioning. a, Size sorting shown in Fig. 2f. **b,** Shape sorting shown in Fig. 2i. **c-d,** Modulus sorting shown in Fig. 2g-h. In each set of images, top left shows the image of particles, and other three show sorting results. Specificity is calculated with the following average number of assembled particles in each trial: 60 (a), 290 (b), 180 (c), and 50 (d).

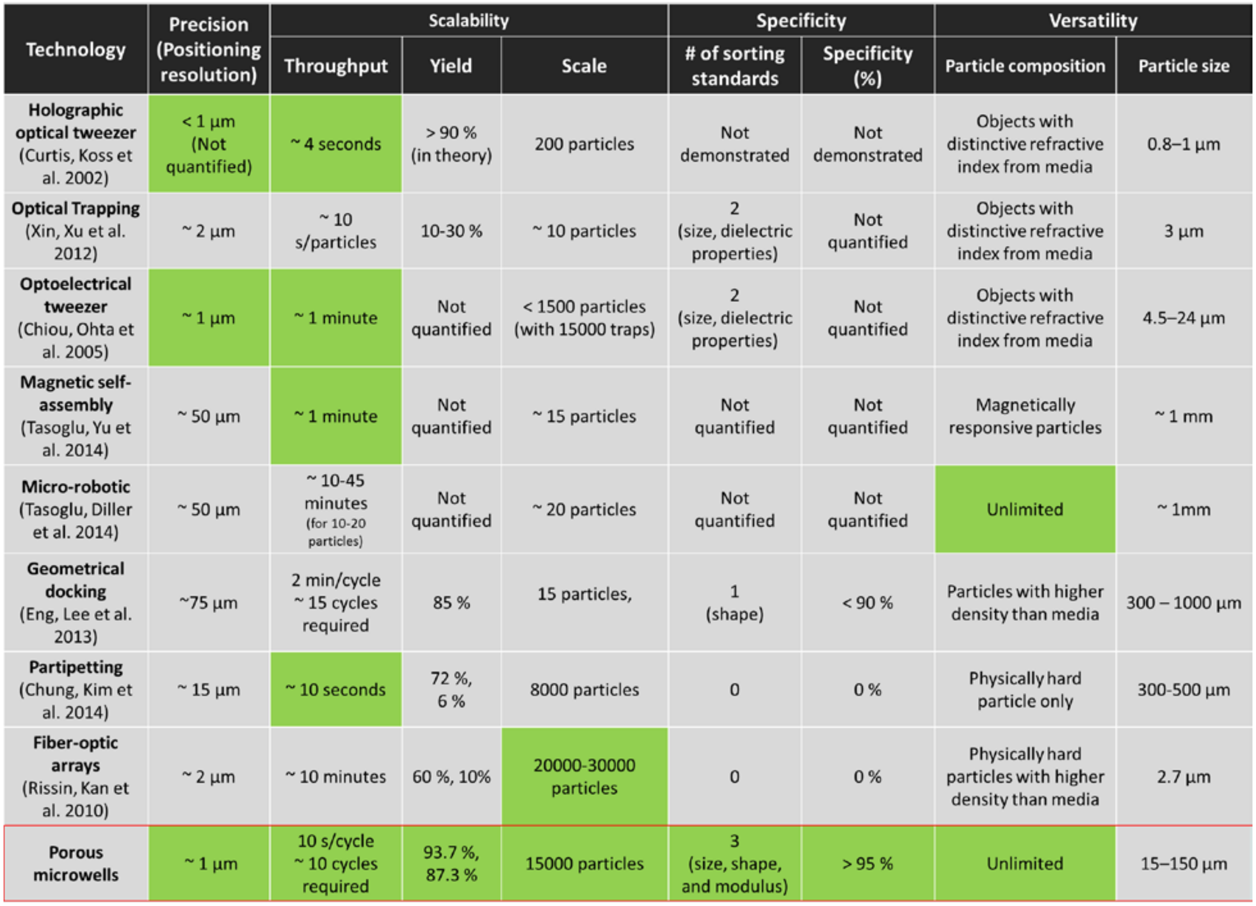

Technology	Precision (Positioning resolution)	Scalability			Specificity		Versatility	
		Throughput	Yield	Scale	# of sorting standards	Specificity (%)	Particle composition	Particle size
Holographic optical tweezer (Curtis, Koss et al. 2002)	< 1 µm (Not quantified)	~ 4 seconds	> 90 % (in theory)	200 particles	Not demonstrated	Not demonstrated	Objects with distinctive refractive index from media	0.8–1 µm
Optical Trapping (Xin, Xu et al. 2012)	~ 2 µm	~ 10 s/particles	10-30 %	~ 10 particles	2 (size, dielectric properties)	Not quantified	Objects with distinctive refractive index from media	3 µm
Optoelectrical tweezer (Chiou, Ohta et al. 2005)	~ 1 µm	~ 1 minute	Not quantified	< 1500 particles (with 15000 traps)	2 (size, dielectric properties)	Not quantified	Objects with distinctive refractive index from media	4.5–24 µm
Magnetic self-assembly (Tasoglu, Yu et al. 2014)	~ 50 µm	~ 1 minute	Not quantified	~ 15 particles	Not quantified	Not quantified	Magnetically responsive particles	~ 1 mm
Micro-robotic (Tasoglu, Diller et al. 2014)	~ 50 µm	~ 10-45 minutes (for 10-20 particles)	Not quantified	~ 20 particles	Not quantified	Not quantified	Unlimited	~ 1mm
Geometrical docking (Eng, Lee et al. 2013)	~75 µm	2 min/cycle ~ 15 cycles required	85 %	15 particles,	1 (shape)	< 90 %	Particles with higher density than media	300 – 1000 µm
Partipetting (Chung, Kim et al. 2014)	~ 15 µm	~ 10 seconds	72 %, 6 %	8000 particles	0	0 %	Physically hard particle only	300-500 µm
Fiber-optic arrays (Rissin, Kan et al. 2010)	~ 2 µm	~ 10 minutes	60 %, 10%	20000-30000 particles	0	0 %	Physically hard particles with higher density than media	2.7 µm
Porous microwells	~ 1 µm	10 s/cycle ~ 10 cycles required	93.7 %, 87.3 %	15000 particles	3 (size, shape, and modulus)	> 95 %	Unlimited	15–150 µm

Table S5. Quantitative comparison of capabilities between various arrangement/sorting technologies. This analysis makes use of reported values in prior studies. In some cases, a parameter was not quantified or demonstrated. Technologies having a capability comparable to or better than porous microwells are shaded as green. If two yields are shown, the first reports the yield of filling(= # of filled microwells/# of total microwells), and the second reports the assembly(= # of assembled particles/# of initially deposited particles). Particle sizes are listed in the table, but not color-coded since there is a not clear size range which is preferred in these technologies.

Movie S1. Movie of transferred UCN-laden microparticle arrays. UCN-laden microparticle arrays, transferred to poker chip surface, were not observed without excitation due to the reflective index matching with coverage. Arrangement of microparticles became observable under the NIR exposure (980 nm). Image is taken by iPhone 5s connected to eyepiece of microscope.

References

1. Wang F, Han Y, Lim CS, Lu YH, Wang J, Xu J, *et al.* Simultaneous phase and size control of upconversion nanocrystals through lanthanide doping. *Nature* 2010, **463**(7284)**:** 1061-1065.

2. Hamrock BJ, Jacobson BO, Schmid SR. *Fundamentals of machine elements*. WCB/McGraw-Hill: Boston, 1999.

3. Guo MY, Wyss HM. Micromechanics of Soft Particles. *Macromol Mater Eng* 2011, **296**(3-4)**:** 223-229.

4. Wyss HM, Franke T, Mele E, Weitz DA. Capillary micromechanics: Measuring the elasticity of microscopic soft objects. *Soft Matter* 2010, **6**(18)**:** 4550-4555.

5. Chapin SC, Pregibon DC, Doyle PS. High-throughput flow alignment of barcoded hydrogel microparticles. *Lab Chip* 2009, **9**(21)**:** 3100-3109.

6. Hwang DK, Oakey J, Toner M, Arthur JA, Anseth KS, Lee S, *et al.* Stop-Flow Lithography for the Production of Shape-Evolving Degradable Microgel Particles. *J Am Chem Soc* 2009, **131**(12)**:** 4499-4504.

7. Dendukuri D, Panda P, Haghgooie R, Kim JM, Hatton TA, Doyle PS. Modeling of Oxygen-Inhibited Free Radical Photopolymerization in a PDMS Microfluidic Device. *Macromolecules* 2008, **41**(22)**:** 8547-8556.

8. Eng G, Lee BW, Parsa H, Chin CD, Schneider J, Linkov G, *et al.* Assembly of complex cell microenvironments using geometrically docked hydrogel shapes. *P Natl Acad Sci USA* 2013, **110**(12)**:** 4551-4556.

9. Zhang L, Zhang F, Yang X, Long GK, Wu YP, Zhang TF, *et al.* Porous 3D graphene-based bulk materials with exceptional high surface area and excellent conductivity for supercapacitors. *Sci Rep-Uk* 2013, **3**.

10. Jiang LL, Fan ZJ. Design of advanced porous graphene materials: from graphene nanomesh to 3D architectures. *Nanoscale* 2014, **6**(4)**:** 1922-1945.